Observation of asymmetric line shapes in precision microwave spectroscopy of the positronium $2\,^3S_1 \rightarrow 2\,^3P_J$ ($J = 1, 2$) fine-structure intervals

L. Gurung,[1] T. J. Babij,[1] J. Pérez-Ríos,[2] S. D. Hogan,[1] and D. B. Cassidy[1]

[1]*Department of Physics and Astronomy, University College London, Gower Street, London WC1E 6BT, United Kingdom*

[2]*Fritz-Haber-Institut der Max-Planck-Gesellschaft, Faradayweg 4-6, 14195 Berlin, Germany*

(Received 29 December 2020; revised 14 March 2021; accepted 15 March 2021; published 5 April 2021)

We report new measurements of the positronium (Ps) $2\,^3S_1 \rightarrow 2\,^3P_J$ fine-structure intervals, ν_J ($J = 0, 1, 2$). In the experiments, Ps atoms, optically excited to the radiatively metastable $2\,^3S_1$ level, flew through microwave radiation fields tuned to drive transitions to the short-lived $2\,^3P_J$ levels, which were detected via the time spectrum of subsequent ground-state Ps annihilation radiation. Both the ν_1 and ν_2 line shapes were found to be asymmetric, which, in the absence of a complete line-shape model, prevents accurate determination of these fine-structure intervals. Conversely, the ν_0 line shape did not exhibit any significant asymmetry; the observed interval, however, was found to disagree with QED theory by 4.2 standard deviations.

DOI: 10.1103/PhysRevA.103.042805

I. INTRODUCTION

Since positronium (Ps), the electron-positron bound state [1], is composed only of leptons, it is free of nuclear structure effects, and practically free of weak interaction effects [2]. As a result, Ps is an ideal system with which to test bound-state QED theory [3], and also to search for possible new physics [4]. Ps wave functions are hydrogenic, scaled by the Ps reduced mass ($\mu_{\rm Ps} = m_e/2$), meaning that the Ps Bohr energy levels are approximately half of the corresponding hydrogen levels. However, the presence of real and virtual annihilation pathways, and a much stronger spin-spin interaction, mean that the Ps fine structure is significantly different from that of hydrogen [5]. Thus, precision measurements of the Ps fine structure can be used to test bound-state QED theory in a manner that is quite distinct [6] from corresponding fine-structure measurements in hydrogen (e.g., [7]).

Figure 1 shows the calculated energy level structure of the ground and first excited states of Ps. Also indicated in Fig. 1 are the lifetimes of each state, which may arise from either radiative or self-annihilation decay processes [8]. The latter requires overlap of the positron and electron wave functions, and is therefore effectively zero for states with orbital angular momentum $\ell > 0$ [5]. Higher-order processes can contribute to the decay of these states, but at experimentally negligible rates [9,10]. Ps radiative lifetimes are approximately twice as long as those of hydrogen, being scaled by the ratio of the respective reduced masses. As with hydrogen and helium, the $2S$ states of Ps are radiatively metastable [11], and in general one can assume that only the $1\,^1S_0$, $1\,^3S_1$, $2\,^1S_0$, and $2\,^3S_1$ levels decay via self-annihilation, and that all others predominantly decay radiatively to the ground state before annihilation occurs.

Ps annihilation decay rates depend strongly on the total spin of the electron-positron pair: the Ps $1\,^1S_0$ (singlet) and $1\,^3S_1$ (triplet) levels have mean lifetimes against annihilation of approximately 125 ps [12] and 142 ns [13,14], respectively. As they depend on the wave-function overlap, annihilation lifetimes scale with n^3, where n is the principal quantum number.

All precision measurements of the Ps $n = 2$ fine-structure intervals performed to date, along with the corresponding calculations, are listed in Table I, from which it is evident that the experimental data are much less precise than the theory. Complete QED calculations of the Ps fine structure have been performed up to order $m_e\alpha^6$, with estimated uncertainties on the order of a few ppm [15,19–21]. Calculations of the $m_e\alpha^7$ corrections are in progress but are not yet complete [22–26].

The previous Ps fine-structure measurements [17,27,28] are more than 25 years old, and one of the goals of the work presented here was to address the long-standing imbalance between experimental and theoretical uncertainties. Recently we reported a new measurement of the ν_0 interval [18]. Although the uncertainty obtained was a factor of 7 smaller than that of the previous best measurement [17], our measurement exhibited a disagreement with theory [15] amounting to $\approx 4.2\sigma$. Here we describe more details of the experimental methods used in that work, and also the results of new measurements of the ν_1 and ν_2 transitions. These new measurements also achieved reduced uncertainties compared to prior work, but both exhibited asymmetric line shapes, precluding an accurate determination of the transition frequencies. Hence, these data are not included in Table I.

II. EXPERIMENTAL METHODS

A. Ps production and excitation

The experimental apparatus and measurement techniques used in this work are explained in detail elsewhere [29–31], and we give only an overview here; a ^{22}Na radioactive source and neon moderator [32] were used to generate a slow positron beam, which was directed into a two-stage Surko-type buffer gas trap [33]. This device produced pulses containing $>10^5$

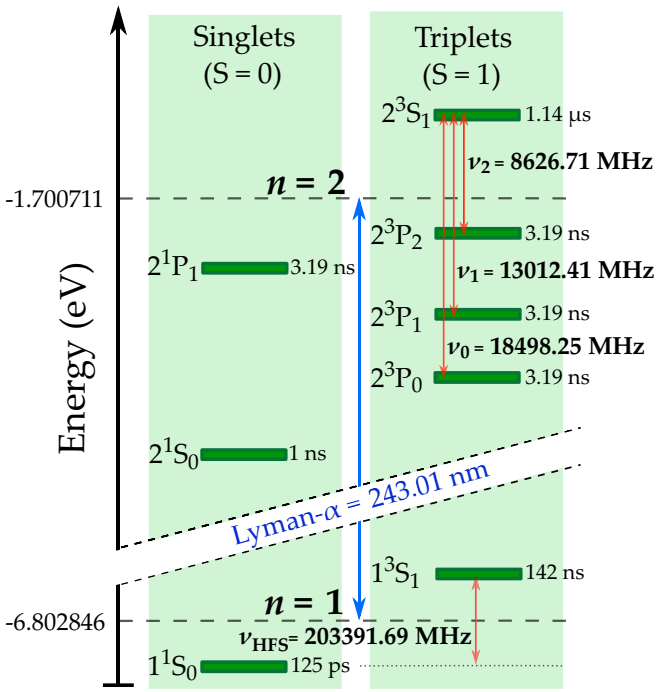

FIG. 1. Energy level diagram of the $n = 1$ and 2 levels in positronium. The energies of the $O(m\alpha^2)$ (Bohr) levels are indicted by the dashed horizontal lines. The calculated transition frequencies for the $n = 1$ hyperfine interval ($\nu_{\rm HFS}$) and the $2\,^3S_1 \to 2\,^3P_J$ ($J = 0, 1, 2$) intervals (ν_J) are also shown [15]. Radiative or annihilation lifetimes for all levels are also indicated, according to the primary decay mode.

positrons with a temporal (spatial) width of 3 ns (2 mm) [full width at half-maximum (FWHM)], at a repetition rate of 1 Hz. The positron beam was guided by an axial magnetic field, and it was implanted into a mesoporous silica target [34] which converted positrons into Ps atoms with an efficiency of ≈30%. With a potential of −3.5 kV applied to the target electrode, ground-state Ps atoms with a mean transverse energy of ≈50 meV were produced [35]. The target electrode was 6 mm away from a parallel grounded waveguide, resulting in a maximum electric field $F_{\rm imp} = 5.8$ kV/cm outside the target during the beam implantation [see Fig. 2(a)].

Transitions from the ground state to $n = 2$ states were achieved by optical excitation using a pulsed ultraviolet (UV) dye laser ($E_{\rm pulse} \approx 0.5$ mJ, $\lambda_{\rm UV} = 243.01$ nm,

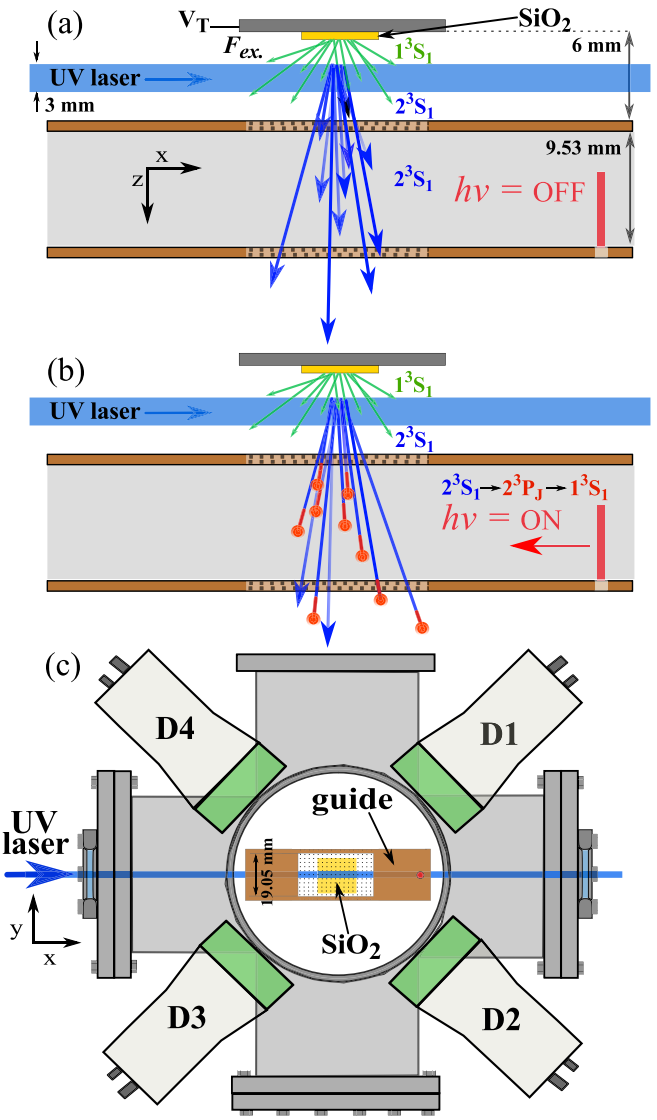

FIG. 2. Schematic of the Ps target, UV laser, and a WR-75 microwave guide with microwave radiation off resonance (a) and on resonance (b). A potential of −3.5 kV was applied to the target electrode (V_T) to control the beam implantation energy. The angular distribution selection in the x direction due to the UV laser bandwidth is also shown. (c) The placement of the four LYSO detectors around the target chamber with respect to the position of the waveguide.

TABLE I. Precision measurements of the $n = 2$ fine-structure intervals, and the corresponding theoretical calculations. Note that the $2\,^3S_1 \to 2\,^1P_1$ transition is strictly forbidden by electric dipole selection rules and C-conjugation invariance, but it can be observed if a magnetic field is present due to Zeeman mixing [16]. The quoted frequency was obtained by extrapolating measurements made in different magnetic fields to the zero-field value (for which the transition strength is zero, in accordance with C invariance). The quoted years refer to the experiments.

Transition	Experiment (MHz)	Precision (Expt.)	Ref.	Year	Theory (MHz)	Precision (Theory)	Ref.
$2\,^3S_1 \to 2\,^1P_1$	$11\,180.0 \pm 5.0_{\rm stat} \pm 4.0_{\rm sys}$	600 ppm	[16]	1993	$11\,185.37 \pm 0.08$	7 ppm	[15]
$2\,^3S_1 \to 2\,^3P_0$	$18\,499.65 \pm 1.20_{\rm stat} \pm 4.00_{\rm sys}$	230 ppm	[17]	1993	$18\,498.25 \pm 0.08$	4 ppm	[15]
$2\,^3S_1 \to 2\,^3P_1$	$13\,012.42 \pm 0.67_{\rm stat} \pm 1.54_{\rm sys}$	130 ppm	[17]	1993	$13\,012.41 \pm 0.08$	6 ppm	[15]
$2\,^3S_1 \to 2\,^3P_2$	$8624.38 \pm 0.54_{\rm stat} \pm 1.40_{\rm sys}$	170 ppm	[17]	1993	8626.71 ± 0.08	10 ppm	[15]
$2\,^3S_1 \to 2\,^3P_0$	$18\,501.02 \pm 0.57_{\rm stat} \pm 0.32_{\rm sys}$	33 ppm	[18]	2020	$18\,498.25 \pm 0.08$	4 ppm	[15]

TABLE II. Specifications of the three waveguides used in the experiments. The dimensions listed refer to the distances between the inner walls in the y, z, and x dimensions (see Fig. 2). The cutoff frequencies refer to the lowest-order TE_{10} modes.

Waveguide	Dimensions (mm)	Range (GHz)	Cutoff (GHz)
WR-51(ν_0)	12.95 × 6.48 × 160	15–22	11.58
WR-75 (ν_1)	19.05 × 9.53 × 160	10–15	7.87
WR-112 (ν_2)	28.5 × 12.6 × 160	7–10	5.26

$\Delta\nu \approx 100$ GHz). The UV laser light was linearly polarized, parallel to the electric and magnetic fields in the excitation region so as to optimize $2\,^3S_1$ production [30]. Additionally, an infrared (IR) dye laser ($E_{\text{pulse}} \approx 2$ mJ, $\lambda_{\text{IR}} = 729$ nm, $\Delta\nu = 5$ GHz) was used to photoionize $n = 2$ atoms in order to perform Doppler scans [29] (see Sec. VI A).

Metastable $2\,^3S_1$ atoms were produced by single-photon optical excitation from the ground state; this transition is forbidden according to electric dipole selection rules [36], but it can be accomplished if the excitation is performed in an electric field. In this case, Stark mixed $n = 2$ states, denoted as $2\,^3S'_1$, are produced. These states possesses both S and P character, allowing the transition to be driven via the $1\,^3S_1 \rightarrow 2\,^3P_J$ pathway. The target bias was turned off after the beam implantation but before the laser excitation, such that $2\,^3S'_1$ atoms were produced in a time-varying electric field [$F = F(t)$], which was approximately 3 kV/cm when the laser was fired and fell to zero within 25 ns, allowing ≈10% of the excited atoms to adiabatically evolve into the pure $2\,^3S_1$ level. This technique is discussed in detail elsewhere [37].

The $2\,^3S_1$ atoms traveled through a waveguide where transitions to the $2\,^3P_J$ levels were driven by microwave radiation via stimulated emission [see Figs. 2(a) and 2(b)]. To probe the individual $\nu_J = 2\,^3S_1 \rightarrow 2\,^3P_J$ ($J = 0, 1, 2$) transitions, three different rectangular waveguides were utilized, the specifications of which are listed in Table II. The center section of the front and back walls of the waveguides was substituted with a tungsten (W) mesh (95% open area) to allow transmission of Ps atoms through the guide. Microwave radiation was introduced into the vacuum system via a high-frequency (45 GHz) UHV feed through, and it was introduced into the waveguides via an antenna so as to propagate in the $-x$ direction, as indicated in Fig. 2(a).

The output from a microwave signal generator (Keysight EXG N5173B) was adjusted to give a constant power level at the waveguide input, P_{input}. Unless otherwise stated, P_{input} was set to be ≈5, 4.3, and 6.4 mW for the ν_0, ν_1, and ν_2 measurements, respectively. The power transmitted through the waveguide was not measured directly, but it was expected to be at least a factor of 2 lower than P_{input}. The polarization of the microwave radiation, determined by the physical structure of the waveguide, was parallel to the magnetic field. Therefore, only the ν_J transitions with $\Delta M_J = 0$ were driven, as indicated in Fig. 3. Also, only TE_{10} modes were able to propagate in the waveguides.

An axial magnetic field B was used to guide the positron beam to the target region. This field could be varied from ≈20 to 100 G, where the lower limit was set by the beam transport efficiency, and the upper limit was determined by the magnet temperature. The guiding field, including contributions from residual fields, was measured using a Hall probe with 1% accuracy. Variation of the field within the waveguides was found to be less than ±1 G, which was therefore used as the uncertainty in the field determination. Since the magnetic field could not be fully eliminated in the experiments, data were taken in a range of magnetic fields, and the obtained Zeeman-shifted transition frequencies were fitted to a quadratic function that was extrapolated to obtain the zero-field values. Zeeman shifts of the individual Ps energy levels were calculated using the methods described in Ref. [30], and they are shown in Fig. 3, with the relevant transitions indicated.

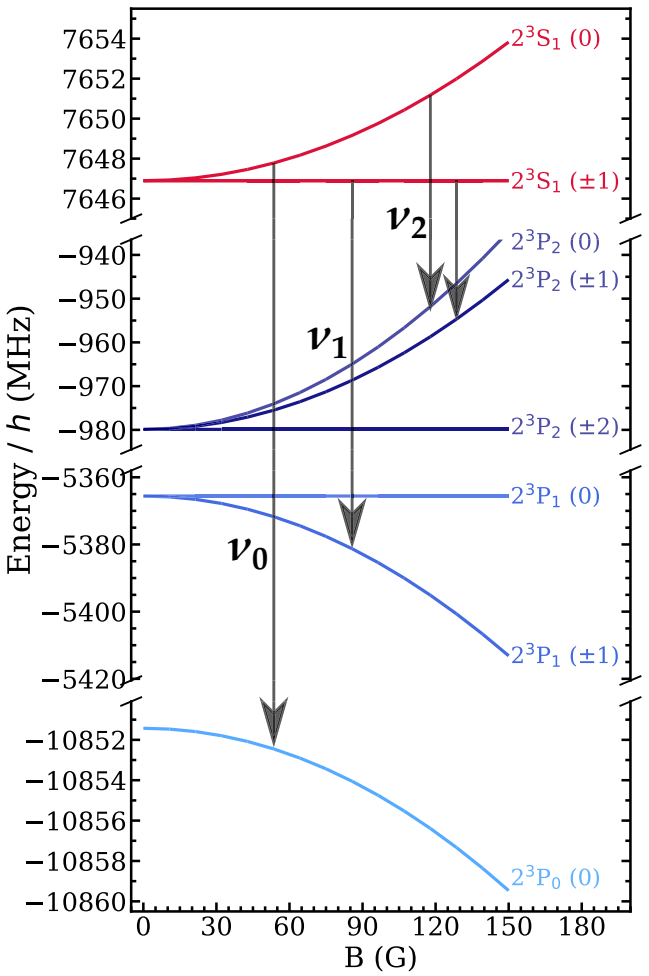

FIG. 3. Zeeman structure of Ps in the $2\,^3S_1(M_J)$ and $2\,^3P_{J=0,1,2}(M_J)$ levels relative to the $n = 2$ Bohr [i.e., $O(m\alpha^2)$] level. The arrows represent the allowed $\Delta M_J = 0$ transitions to the $2\,^3P_J$ states. Note the different energy scales of the various sections in this figure.

B. Ps detection

The production and excitation of Ps was monitored via the time dependence of its annihilation γ radiation using a single shot lifetime technique [38]. After a positron pulse was implanted into the silica target, the emission of annihilation

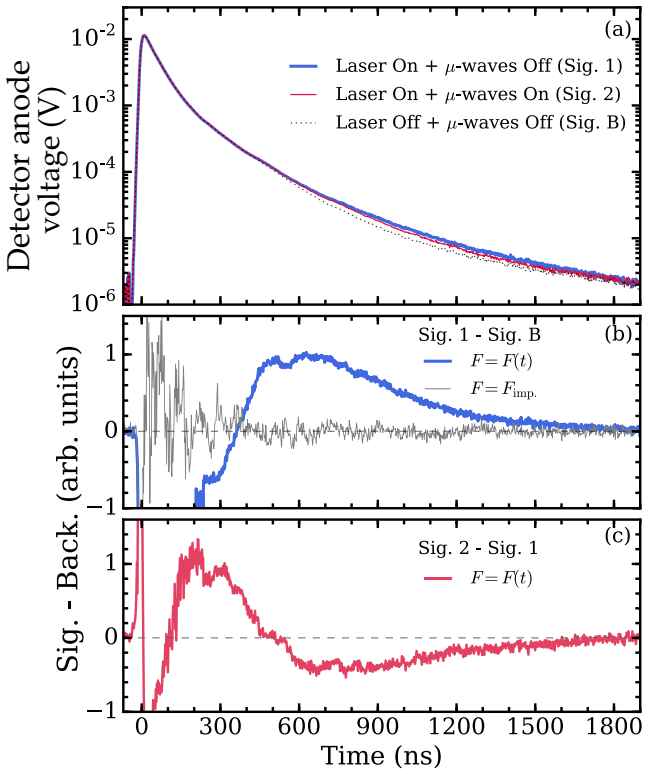

FIG. 4. (a) Lifetime spectra measured using D4 for three cases as outlined in the text. (b) Difference spectra demonstrating $2\,^3S_1$ production (Sig. 1–Sig. B) with and without the electric field switched off after the positron beam has been implanted into the silica target, as indicated. (c) Difference spectrum demonstrating the microwave radiation induced ν_2 transition (Sig. 2–Sig. 1).

γ radiation was measured using four lutetium yttrium oxyorthosilicate (LYSO) scintillator based γ-ray detectors [30]. The detectors, labeled D1–D4, were placed around the chamber so as to be symmetrically equidistant from the excitation region, as indicated in Fig. 2(c). The time-dependent γ-ray flux constitutes a lifetime spectrum, convoluted with the detector response [39]. Examples of lifetime spectra are shown in Fig. 4(a) for three cases; Sig. 1 refers to measurements made with the UV laser tuned to the $1\,^3S_1 \rightarrow 2\,^3P_J$ resonance and the μ-wave radiation off resonance; Sig. 2 refers to measurements made with the UV laser on resonance and the μ-wave radiation tuned to drive the $2\,^3S_1 \rightarrow 2\,^3P_2$ transition; Sig. B refers to measurements made when both the UV and microwave radiation were off resonance.

Lifetime spectra may be parameterized by the quantity

$$f_{\rm d} = \int_B^C V(t)\,dt \Big/ \int_A^C V(t)\,dt, \tag{1}$$

where $V(t)$ is the detector output voltage, and $(A, B, C) = (-30, 700, 1400)$ ns define the integration time windows used in this work [29]; these windows are chosen so as to optimize the signal-to-noise ratio [39]. If the lifetime of Ps atoms changes following, for example, interactions with radiation, then $f_{\rm d}$ will also change. Changes of this type can be directly observed via difference spectra, obtained by subtracting one case from another, as shown in Figs. 4(b) and 4(c). Such effects can be parametrized by the quantity S_γ, defined as

$$S_\gamma = \frac{f_{\rm off} - f_{\rm on}}{f_{\rm off}}, \tag{2}$$

where $f_{\rm on}$ and $f_{\rm off}$ refer here to the measurement with microwave radiation on and off resonance, respectively.

Difference curves for spectra with UV radiation on and off resonance (Sig. 1–Sig. B) are shown in Fig. 4(b). Two cases are shown, with the electric field $F_{\rm imp}$ turned off after implantation of the positron beam [$F = F(t)$], and also when the field was left on ($F = F_{\rm imp}$). The difference spectra show the time profile of Ps annihilation events relative to that of ground-state atoms. Thus, when $2\,^3S_1$ atoms were produced [$F = F(t)$], the spectrum exhibited a peak at late times ($\approx$600 ns). No such peak was observed when the excited atoms were able to rapidly decay to the ground state ($F = F_{\rm imp}$).

Figure 4(c) shows a difference spectrum obtained when $2\,^3S_1$ atoms were produced [$F = F(t)$] with resonant microwave radiation present. In this case, a delayed excess annihilation peak was present, but it occurred earlier ($\approx$300 ns), at a time corresponding to the arrival of atoms in the waveguide and their subsequent decay after being driven to the $2\,^3P_2$ level.

III. LINE-SHAPE FITTING

Spectral line shapes were generated by measuring S_γ as a function of the microwave frequency with the same experimental conditions used to obtain the data shown in Fig. 4(c), but with the microwave radiation tuned through the resonance frequency. In the absence of perturbing or broadening effects, spectral line shapes can be described using Lorentzian profiles of the form

$$L(\nu) = \frac{2A/\pi\Gamma_0}{1 + 4[(\nu - \nu_{\rm R})/\Gamma_{\rm m}]^2}, \tag{3}$$

where A is a constant, and $\nu_{\rm R}$ and $\Gamma_{\rm m}$ are the resonance frequency and the measured linewidth (FWHM), respectively. One can generate more complicated line shapes that take into account the details of the excitation process [28], but in general if the line shape is symmetric, then any suitable symmetric function can be used to obtain the center frequency, which will correspond to the resonance frequency unless the entire line is shifted. Symmetric profiles cannot, however, account for any asymmetric perturbations that may occur, for example via interference effects.

One can determine the extent to which a measured line shape is asymmetric by fitting using a spectral profile with a built-in asymmetry component. However, unless these profile models are developed so as to include all relevant processes, this approach does not allow extraction of the true resonance frequency. Nevertheless, it can reveal whether or not a line shape is in fact asymmetric, and thus indicate whether it is appropriate to use a symmetric function to describe it or not. Several asymmetric line-shape models have been developed (e.g., [40]). Here we use a Fano profile [41] of the form

$$F(\nu) = A\left[\frac{(q+\epsilon)^2}{(1+q^2)(1+\epsilon^2)}\right]. \tag{4}$$

Here A is a constant, q is a parameter that characterizes the asymmetry, and $\epsilon = (\nu - \nu_R)/\Gamma_m$ is the reduced energy, where ν_R is the Fano resonance frequency and Γ_m is the Lorentzian FWHM. In the limit $q \to \infty$, the Fano profile becomes a Lorentz function, while for $q = 0$ it reduces to a symmetric antiresonance. For $q < 0$ ($q > 0$), the Fano profile is asymmetric and is skewed toward lower (higher) frequencies. This function, originally developed to describe interference between resonant and continuum electron scattering in helium [41], can also represent more general interference phenomena, and therefore finds application in many different areas of physics (e.g., [42,43]).

In this work, the Fano function was used only to determine if line shapes were asymmetric or not; the ability to fit asymmetric data well does not mean that ν_R corresponds to the true resonance frequency. To obtain the resonance frequencies, is it is necessary to develop a compete line-shape model that properly takes into account the mechanism(s) leading to the asymmetry. It is of course possible to obtain the frequency at which the Fano profile has its maximum value simply by taking its derivative (in practice, we use equivalent algorithms for faster processing [44]). This is also not expected to yield the true resonance frequency, but it may be closer to it than ν_R in cases in which the perturbing effects on the line shape are small, and the linewidth is relatively large, as in the present work.

IV. RESULTS

Line shapes for the ν_J transitions were generated by measuring S_γ (see Sec. II B) as a function of the microwave frequency ν; example line shapes, obtained in a magnetic field of 32 G using detector D4 (see Fig. 2), are shown in Fig. 5. The ν_R, q, and Γ_m values were consistent across the four detectors used in the experiment, and all measured quantities from each of the detectors were averaged to produce the final results.

Different waveguides were used for each of the three transitions studied; their properties are summarized in Table II. The relationship between the electric field strength E and the power P in a waveguide is different from that in free space [17]. Therefore, the measured line shapes required a correction of the form $E^2 \sim P(1 - \nu_c^2/\nu^2)^{-1/2}$, where ν_c are the lowest-order cutoff frequencies for the waveguides used in the measurements (see Table II). This procedure amounted to a negligible correction of ≈20 kHz to the ν_R values, while the Γ_0 and q values were unaffected.

The physical structure and orientation of the waveguides was such that the microwave radiation was polarized parallel to the magnetic field (see Fig. 2), meaning that to a first approximation only $\Delta M_J = 0$ electric dipole transitions were driven by the microwave radiation. Spontaneous radiative decay from the $2\,^3P_J$ levels, however, could proceed via both $\Delta M_J = 0$ and ± 1 transitions, as indicated in the insets of Fig. 5. The $\Delta M_J = 0$ requirement for the microwave transitions meant that the ν_2 signal was the strongest, as all three $2\,^3S_1$ sublevels could be depopulated, whereas the ν_1 and ν_0 transitions were weaker, as fewer sublevels were depopulated. Taking into account the transition strengths, one would expect relative signal intensities of 5:3:1 for the $\nu_2 : \nu_1 : \nu_0$ transitions (see Sec. V). However, since the three measurements

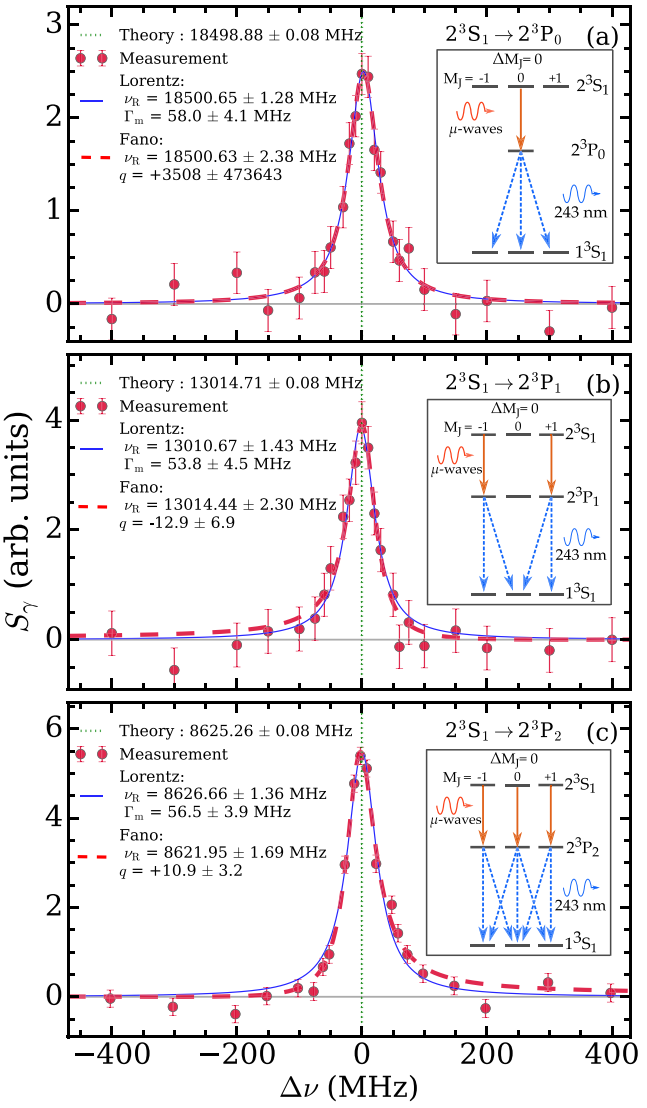

FIG. 5. Example line shapes of the ν_0 (a), ν_1 (b), and ν_2 (c) transitions, measured in a magnetic field of 32 G using detector D4. Both Lorentzian and Fano fits were applied to all line shapes. The dotted (green) vertical lines at $\Delta\nu = 0$ indicate the Zeeman-shifted theoretical transition frequencies, shown in the legends. The insets show the allowed $\Delta M_J = 0$ transitions (solid arrows) to the $2\,^3P_J$ states, followed by $\Delta M_J = 0, \pm 1$ radiative decay (dashed arrows) to the ground state.

were not performed under identical conditions, we do not observe exactly these ratios.

The mean radiative lifetime in the $2\,^3P_J$ states is $\tau_{rad} = 3.19$ ns [5]. Therefore, the natural linewidth of all the ν_J transitions is $\Gamma_0 = 1/2\pi\tau_{rad} \approx 50$ MHz. As discussed below, the *measured* line shapes all had widths $\Gamma_m > \Gamma_0$. The data in Fig. 5 were fitted with a Lorentzian profile as described in Sec. III from which we obtain $\nu_0 = 18\,500.65 \pm 1.28$ MHz, $\nu_1 = 13\,010.67 \pm 1.43$ MHz, and $\nu_2 = 8626.66 \pm 1.36$ MHz. The data in Fig. 5 were also fitted using the Fano profile, as described in Sec. III. From these fits, we obtain q values that quantify asymmetry in the corresponding line shapes. For these particular data, we find that for the ν_0 transition,

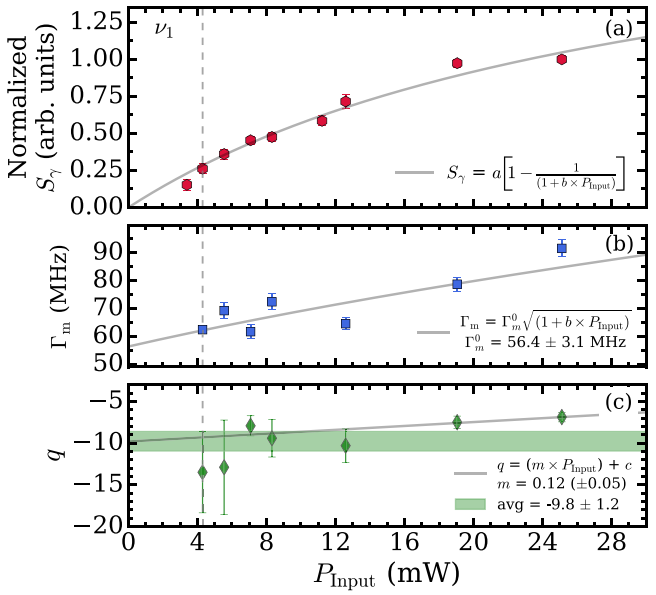

FIG. 6. (a) The microwave-induced transition signal, S_γ, measured on resonance for different applied microwave powers. (b) Measured linewidths Γ_m obtained from Lorentz fits and (c) Fano asymmetry parameter q, obtained from Fano fits to data measured as a function of applied microwave power. The curves in each panel are fits to the functions shown in the corresponding legends, as explained in the text. These measurements were made for the ν_1 transition in a magnetic field of 82 G. The vertical dashed line indicates the power (4.3 mW) at which the ν_1 data presented elsewhere in this article were recorded.

q is ≈30 000, indicating essentially no asymmetry. However, the ν_1 and ν_2 line shapes have q values of approximately −13 and +11, respectively, indicating similarly asymmetric lines, skewed in opposite directions. The resonant frequencies (ν_R) obtained from the Fano fits were 18 500.63 ± 2.38, 13 014.44 ± 2.30, and 8621.95 ± 1.69 MHz for the ν_0, ν_1, and ν_2 transitions, respectively.

The ν_0 Fano line shape is essentially identical to the Lorentz fit, as expected from the large q value. However, the ν_1 (ν_2) line shape is asymmetric and skewed toward higher (lower) frequencies, as indicated by the respective q values. While the asymmetry observed for both line shapes may be small, the extracted resonance frequencies from the two fits are nevertheless significantly different, with the Fano results deviating from the Lorentzian results by +3.77 and −4.71 MHz for the ν_1 and ν_2 transitions, respectively (for these particular measurements). Although neither the Lorentzian nor the Fano profiles can be expected to yield the correct resonance frequencies if the line shape is asymmetric, the difference between the frequencies obtained from each of them indicates the extent to which apparent shifts can occur.

To verify that the microwave power used was not saturating the transitions, line shapes were measured for different input powers, $P_{\rm input}$. The maximum S_γ values obtained are shown in Fig. 6(a) for the ν_1 transition; similar measurements were made for the other transitions. Increasing the microwave power increases the signal, with the value of $P_{\rm input}$ that results in saturation obtained by fitting the function [45]

$$S_\gamma = a\left[1 - \frac{1}{1 + b\,P_{\rm input}}\right] \tag{5}$$

to the data. In this expression, a and b are free fit parameters, and the quantity $b\,P_{\rm input}$ represents the saturation parameter, i.e., the ratio of the microwave intensity in the waveguide to the saturation intensity. From this fit, represented by the gray curve in Fig. 6(a), $b = 0.0322 \pm 0.0087$ mW^{-1}. Since saturation occurs when $b\,P_{\rm input} > 1$, in this case the transition will become saturated when $P_{\rm input} \gtrsim 30 \pm 8$ mW.

As $P_{\rm input}$ was increased, the measured linewidths $\Gamma_{\rm m}$ also increased from ≈60 to 90 MHz, as shown in Fig. 6(b), where the widths were obtained from Lorentzian fits; the corresponding widths obtained from Fano fits were found to be almost identical. These data allowed a separate determination of the value of $P_{\rm input}$ that resulted in saturation, by fitting the function

$$\Gamma_{\rm m} = \Gamma_{\rm m}^0\sqrt{1 + b\,P_{\rm input}}, \tag{6}$$

where $\Gamma_{\rm m}^0$, the measured width extrapolated to zero power, and b were free fit parameters. Here again $b\,P_{\rm input}$ is the saturation parameter. From this fit, represented by the gray curve in Fig. 6(b), we obtain $b = 0.0504 \pm 0.0179$ mW^{-1}, and saturation will therefore occur for $P_{\rm input} \gtrsim 20 \pm 7$ mW, which is consistent with the direct saturation measurements in Fig. 6(a). The increased linewidths for higher power are attributed to power broadening [45], but $\Gamma_{\rm m}^0$ remains greater than Γ_0, indicating that there exists another, power-independent, source of broadening. To minimize power broadening, measurements of the ν_0, ν_1, and ν_2 transitions were made with $P_{\rm input} = 5$, 4.3, and 6.5 mW, respectively.

Ps atoms with mean longitudinal speeds $v_z^{\rm rms} = 10^7$ cm/s [46] will have mean flight times through the three waveguides ranging from 65 to 120 ns (see Table II). This must be combined with the spatial distribution of the microwave field strength within the guide to determine the effective time dependence of the microwave field experienced by the atoms, and hence the transit time broadening. Moreover, there is a significant spread in the velocity distributions (on the order of 25% [46]), meaning that there will be a corresponding range of effective flight times through the microwave field. This gives rise to possible transit time contributions ranging from ≈8 to 15 MHz, which, along with the 50 MHz natural width, is consistent with the observed linewidths.

The q values obtained from the Fano fits at different $P_{\rm input}$ values are shown in Fig. 6(c). It can be seen that the asymmetry does not disappear for low power, and is not significantly different at high powers. As indicated in the figure, a linear fit was made to the $\Gamma_{\rm m}$ and q values, as a crude metric of power dependence. These fits indicate that the width depends in general on the power (as expected), and that the asymmetry also appears to exhibit a weak power dependence.

The experiments reported here were performed in an axial magnetic field, and therefore Zeeman shifts of the $n = 2$ energy levels had to be taken into account. To do this, line shapes were measured in a range of magnetic fields, as shown in Fig. 7. Each line shape was fitted with both Lorentzian and Fano profiles, and the ν_R values from these fits are shown in the figure. Each individual data point is the average of the

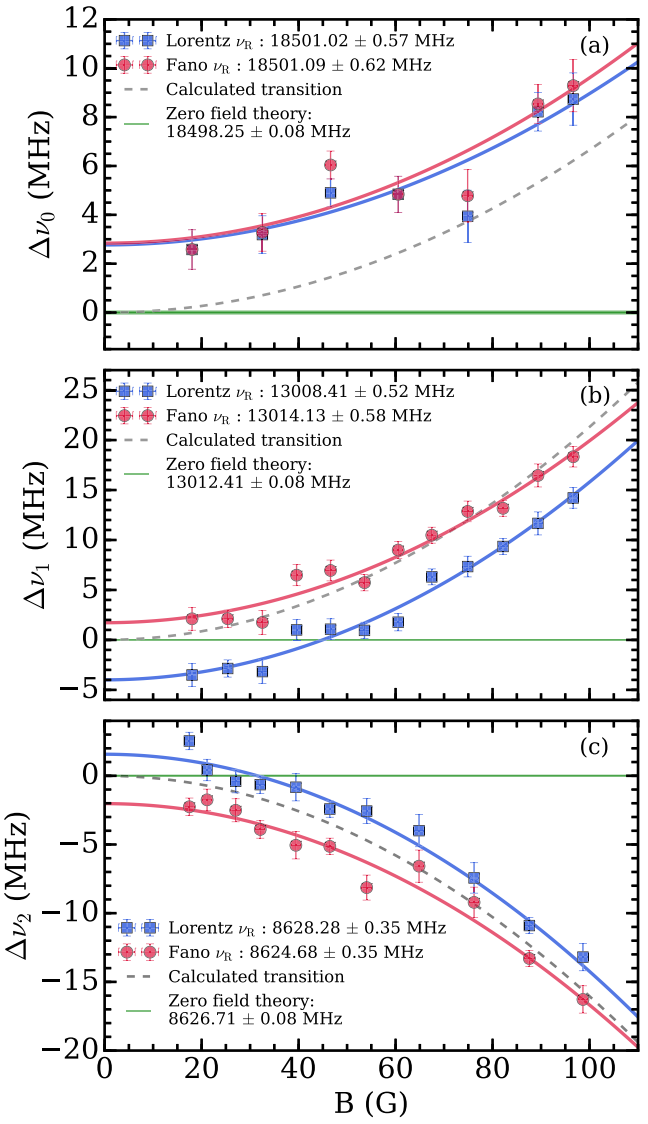

FIG. 7. The ν_0 (a), ν_1 (b), and ν_2 (c) transition frequencies, relative to the calculated zero-field frequencies, measured in different magnetic fields. The ν_R values from Lorentz and Fano fits to the line shapes are indicated by the blue squares and red circles, respectively, and the quadratic fits are indicated by the solid curves. The calculated transition frequencies as a function of the magnetic field are represented by the dashed lines. In the case of the ν_2 transition, the dashed line represents the average of the two individual $\Delta M_J = 0$ transitions, weighted by the relative transition strengths.

ν_R measurements obtained from all four detectors. Fitting a quadratic function of the form $y = aB^2 + c$ to the data in Fig. 7 allows extrapolation to the zero magnetic field value by determining the intercept c. The calculated and measured a coefficients are listed in Table III for both Lorentzian and Fano fits. Also shown are the measured c parameters used to determine the zero-field transition frequencies (the calculated c intercepts are zero by definition).

From the Lorentzian fits, we obtain zero-field resonance frequencies of 18 501.02 ± 0.57, 13 008.41 ± 0.52, and 8628.28 ± 0.35 MHz for the ν_0, ν_1, and ν_2 transitions, respectively. Using the Fano spectral profile, we obtain field

TABLE III. Calculated and measured parameters of the Zeeman shifts shown in Fig. 7 for both Lorentzian and Fano fitting, as indicated. The parameters a_{calc} and a_{fit} refer to the a coefficients in the quadratic curves obtained from a calculation, and from fitting the data, respectively, and c_{fit} is the measured zero-field intercept. The corresponding intercept for the calculated curves (c_{calc}) is zero by definition.

Transition	a_{calc} (MHz/G^2)	a_{fit} (MHz/G^2)	c_{fit} (MHz)
ν_0 (Lorentz)	6.7×10^{-4}	$(6.2 \pm 1.2) \times 10^{-4}$	2.77
ν_0 (Fano)	6.7×10^{-4}	$(6.8 \pm 1.5) \times 10^{-4}$	2.84
ν_1 (Lorentz)	1.5×10^{-3}	$(1.9 \pm 0.1) \times 10^{-3}$	−4.00
ν_1 (Fano)	1.5×10^{-3}	$(1.8 \pm 0.1) \times 10^{-3}$	1.72
ν_2 (Lorentz)	-1.6×10^{-3}	$(-0.6 \pm 0.1) \times 10^{-3}$	1.57
ν_2 (Fano)	-1.6×10^{-3}	$(-1.5 \pm 0.1) \times 10^{-3}$	−2.03

free frequencies of 18 501.09 ± 0.52, 13 014.13 ± 0.58, and 8624.688 ± 0.35 MHz for the same transitions. The quoted uncertainties are statistical, and are due primarily to the statistical errors of the individual data points. It is evident that the ν_0 data are almost identical for the Lorentzian and Fano fits, as expected for a symmetric line shape. The ν_1 and ν_2 Lorentzian and Fano data, however, are significantly different, and are shifted in opposite directions with respect to the calculated Zeeman-shifted resonance frequencies, which are indicated in Fig. 7 by the dashed lines.

Although the Zeeman shifts of the transition frequencies are significant over the range of fields studied (see Fig. 3), there is no reason to expect the lines to become broader in higher magnetic fields. There could be a small broadening in the ν_2 transition since this line is actually composed of two unresolved components [i.e., the $2\,^3S_1(0) \rightarrow 2\,^3P_2(0)$ and $2\,^3S_1(\pm1) \rightarrow 2\,^3P_2(\pm1)$ transitions] with slightly different Zeeman shifts. However, these shifts are in the same direction in both cases, and the separation between them is less than 5 MHz at the highest fields studied.

Figure 8 shows the linewidths of the ν_0, ν_1, and ν_2 transitions measured in different magnetic fields. These widths were obtained by fitting Lorentzian functions. Linear fits have again been applied to the data to provide a rough metric of field dependence. The fits suggest that there may be a weak-field dependence for the ν_0 measurements, with none apparent for the ν_1 and ν_2 transitions. The average linewidths obtained for all magnetic fields is also shown in the figure. The field-averaged values of Γ_m are 66.2 ± 1.0, 62.4 ± 0.9, and 61.8 ± 0.7 MHz for the ν_0, ν_1, and ν_2 transitions, respectively. As discussed above, these linewidths are attributed to a combination of the finite lifetime of the $2P$ levels and transit time broadening. We note that the observed excess widths above Γ_0 do not scale with the physical dimensions of the relevant waveguides because the transition rates therein are not all the same.

The Fano q values obtained from the measurements performed at different magnetic fields are shown in Fig. 9. Linear fits were applied and reveal no significant magnetic field dependence of the q values for any of the transitions. The field-averaged values of q are $+2 \times 10^5 \pm 20$, -13.7 ± 1.7, and $+19.5 \pm 2$ for the ν_0, ν_1, and ν_2 transitions, respectively. Large q values on the order of 10^5 fully justify the use of

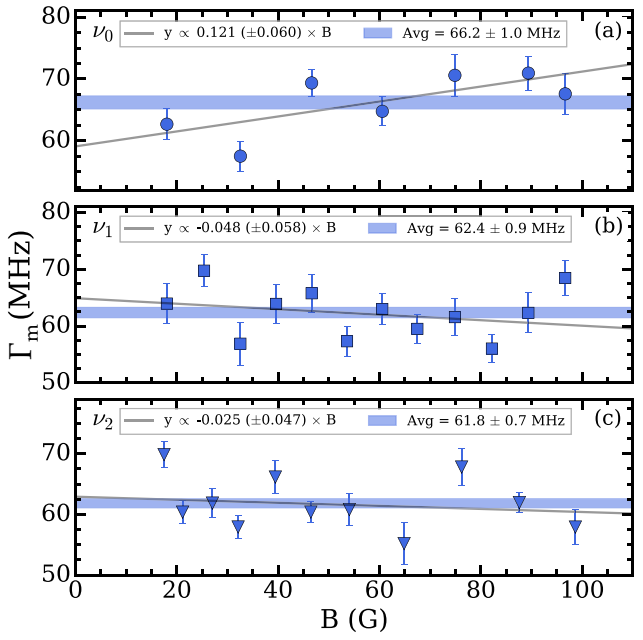

FIG. 8. The measured Lorentz linewidths Γ_m for the ν_0 (a), ν_1 (b), and ν_2 (c) transitions as a function of the magnetic field B. The horizontal shaded bars represent the average value of Γ_m, and the solid lines represent a linear fit to the data.

Lorentzian profiles to describe the resonance frequency of the ν_0 spectrum. Conversely, the much smaller magnitude of the q values obtained for the other transitions means that Lorentzian profiles are not suitable for fitting these data.

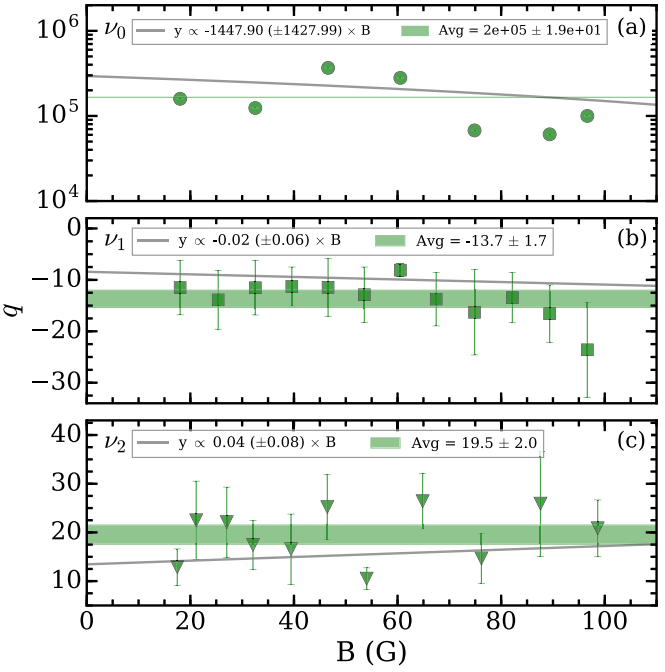

FIG. 9. The measured Fano asymmetry parameter, q, for the ν_0 (a), ν_1 (b), and ν_2 (c) transitions as a function of the magnetic field B. The horizontal shaded bars represents the average value of q, and the line represent a linear fit to the data.

V. QUANTUM INTERFERENCE

One possible explanation for the asymmetric ν_1 and ν_2 line shapes and the ν_0 shift is the influence of neighboring resonances on the transitions being studied [47]. In a number of recent high-precision spectroscopic measurements [48–54], it has become apparent that quantum interference (QI) effects can lead to significant shifts in the observed transition frequencies. For precision measurements, these effects cannot be overlooked, and indeed a number of previously discrepant measurements of the fine structure of helium are now in agreement after the application of appropriate QI-based adjustments [55].

There are many different ways in which QI effects can manifest in precision spectroscopy, and the details are specific to the particular experimental arrangement used. Generally, the presence of a nearby state provides an off-resonant pathway that can interfere with a resonant transition. The amplitude of the off-resonant component may be small compared to that of the near-resonant transition, but the effect on the line shape may nevertheless be significant. Moreover, these effects may be subtle, and they will not necessarily result in an asymmetric line shape [56].

Hessels and co-workers have made significant contributions toward understanding these effects [47,56–59], and they have shown that measurements performed with an uncertainty comparable to the square of the linewidth divided by (twice) the separation of the main resonance and a neighboring (off-resonant) transition may well be affected by them [55]. This "rule of thumb" [47], which has also been obtained analytically by other researchers using perturbation theory [60], gives an approximate value for the error one would obtain fitting a Lorentzian profile to a line shape distorted by QI effects. We note that in some types of measurements, line shapes are distorted via direct interference between incident and emitted radiation (e.g., [49,52]). The present experiments are not susceptible to these effects since the number of surviving atoms is measured via the time dependence of their annihilation radiation.

Thus, for a resonant transition to a particular state, with another electric-dipole-allowed (off-resonant) pathway to a second state separated by a detuning Δ, the expected shift ($\Delta\nu$) due to QI may be approximated by $\Delta\nu \approx \Gamma_m^2/2\Delta$, assuming that both transitions have the same linewidth Γ_m. In the case of the ν_0 transition of interest here, the off-resonant $2\,^3S_1(0) \rightarrow 2\,^3P_1(0)$ transition is forbidden by electric dipole selection rules and, therefore, is not expected to affect the ν_0 line center. The $2\,^3S_1(0) \rightarrow 2\,^3P_0(0)$ and $2\,^3S_1(0) \rightarrow 2\,^3P_2(0)$ transitions both have measured linewidths of ≈60 MHz, and they are separated by $\Delta \approx 10$ GHz. The shift in the ν_0 resonance frequency due to the interference from the off-resonant ν_2 pathway is then expected to be ≈180 kHz, which is much smaller than the observed 2.77 MHz discrepancy with theory.

The separation between the $2\,^3S_1(\pm1) \rightarrow 2\,^3P_1(\pm1)$ and $2\,^3S_1(\pm1) \rightarrow 2\,^3P_2(\pm1)$ transition frequencies is 4.4 GHz. The expected shift in the ν_1 resonance due to the off-resonant ν_2 pathway will therefore be ≈400 kHz, which is also too small to account for the ≈2–4 MHz shift, for the Lorentz cases, as seen in Fig. 7(b). The ν_2 resonance is expected to be similarly shifted by ≈400 kHz due to the nearby ν_0 and ν_1 pathways.

It is worth noting, however, that the asymmetry in the ν_1 and ν_2 line shapes is qualitatively consistent with effects arising from the neighboring lines insofar as the lines are skewed toward each other. Similarly, the symmetric ν_0 line shape is consistent with the fact that the corresponding ν_1 transition (i.e., $M_J = 0 \rightarrow M_J = 0$) is suppressed.

To evaluate more precisely effects of QI on the particular transitions studied here, numerical calculations were performed to follow the time evolution of the excited-state population under the experimental conditions. In this treatment, solutions to the Lindblad master equation [61,62]

$$\hbar\frac{\partial\rho}{\partial t} = -i[H(t),\rho\,] + \cdots + \sum_k \Gamma_k\left(L_k\rho L_k^\dagger - \frac{L_k^\dagger L_k\rho}{2} - \frac{\rho L_k^\dagger L_k}{2}\right) \quad (7)$$

were obtained within the density matrix formalism (as, for example, reported in Ref. [56]), where $H(t)$ is a time-dependent Hamiltonian, ρ is the density operator, and L_k represent collapse operators that account for dissipation and decoherence. These calculations were performed using the open-source Python framework QuTiP [63].

Since the linearly polarized microwave field propagating through the waveguides in the experiments coupled states for which $\Delta M_J = 0$, the spectral line shape associated with each $2\,^3S_1 \rightarrow 2\,^3P_J$ transition was calculated with a set of four basis states. These states were (i) the initial $2\,^3S_1$ level, (ii) the $2\,^3P_J$ level to which the microwave transition was driven near resonance, (iii) the off-resonant $2\,^3P_{J'}$ level that contributes to effects of QI, and (iv) the $1\,^3S_1$ ground level to which the $2\,^3P_J$ and $2\,^3P_{J'}$ levels both radiatively decay.

The Hamiltonian $H(t)$ describing the interaction of this four-level system with a microwave field at an angular frequency $\omega_\mu = 2\pi\,\nu_\mu$ can be expressed in matrix form, with the basis states arranged in the order listed above, and the diagonal elements included as angular frequencies with respect to the $2\,^3S_1$ level, as

$$H(t) = \hbar\begin{pmatrix} 0 & \frac{1}{2}\Omega_{2S,\,2P_J}(t) & \frac{1}{2}\Omega_{2S,\,2P_{J'}}(t) & 0 \\ \frac{1}{2}\Omega_{2S,\,2P_J}(t) & -\omega_{2P_J}+\omega_\mu & 0 & 0 \\ \frac{1}{2}\Omega_{2S,\,2P_{J'}}(t) & 0 & -\omega_{2P_{J'}}+\omega_\mu & 0 \\ 0 & 0 & 0 & -\omega_{1S} \end{pmatrix}. \quad (8)$$

In this expression, the frequency intervals and time-dependent electric dipole couplings—Rabi frequencies—between the $2\,^3S_1$ and $2\,^3P_J$ ($2\,^3S_1$ and $2\,^3P_{J'}$) levels are denoted ω_{2P_J} ($\omega_{2P_{J'}}$) and $\Omega_{2S,\,2P_J}(t)$ [$\Omega_{2S,\,2P_{J'}}(t)$], respectively. The electric dipole transition moments $d_{2S,\,2P_J}$ and $d_{2S,\,2P_{J'}}$ required to calculate the corresponding Rabi frequencies are given in Table IV. Since the interval between the uncoupled $2\,^3S_1$ and $1\,^3S_1$ levels, i.e., $\omega_{1S} = 2\pi \times 1234$ THz, is much greater than ω_{2P_J} or $\omega_{2P_{J'}}$, which lie between $2\pi \times 8.6$ and $2\pi \times 18.5$ GHz, the microwave dressing of the diagonal matrix element representing the energy of the $1\,^3S_1$ level was neglected.

TABLE IV. Electric dipole moments, $d_{2S_1,\,2P_J}$, associated with the $2\,^3S_1(M_J) \rightarrow 2\,^3P_J(M_J)$ transitions in Ps. In each case, the radial part of the transition moment is denoted $\mathcal{R}_{2S,\,2P} = 5.196\,e\,a_{\rm Ps}$.

Transition	Initial state $2\,^3S_1(M_J)$	Final state $2\,^3P_J(M_J)$	Transition moment $d_{2S_1,\,2P_J}$
ν_0	$2\,^3S_1(0)$	$2\,^3P_0(0)$	$-\frac{1}{3}\,\mathcal{R}_{2S,\,2P}$
	$2\,^3S_1(0)$	$2\,^3P_2(0)$	$+\frac{\sqrt{2}}{3}\,\mathcal{R}_{2S,\,2P}$
ν_1	$2\,^3S_1(1)$	$2\,^3P_1(1)$	$-\frac{1}{\sqrt{6}}\,\mathcal{R}_{2S,\,2P}$
	$2\,^3S_1(1)$	$2\,^3P_2(1)$	$+\frac{1}{\sqrt{6}}\,\mathcal{R}_{2S,\,2P}$
$\nu_{2(M_J=0)}$	$2\,^3S_1(0)$	$2\,^3P_2(0)$	$+\frac{\sqrt{2}}{3}\,\mathcal{R}_{2S,\,2P}$
	$2\,^3S_1(0)$	$2\,^3P_0(0)$	$-\frac{1}{3}\,\mathcal{R}_{2S,\,2P}$
$\nu_{2(M_J=1)}$	$2\,^3S_1(1)$	$2\,^3P_2(1)$	$+\frac{1}{\sqrt{6}}\,\mathcal{R}_{2S,\,2P}$
	$2\,^3S_1(1)$	$2\,^3P_1(1)$	$-\frac{1}{\sqrt{6}}\,\mathcal{R}_{2S,\,2P}$

The finite interaction time of the atoms with the microwave field as they traveled through the waveguides in the experiments was accounted for in the calculations through the time dependence of the microwave field strength, and hence the Rabi frequencies $\Omega_{2S,\,2P_J}(t)$ and $\Omega_{2S,\,2P_{J'}}(t)$. The total interaction time of the atoms with the microwave field was set to $T_{\rm int} = 100$, 140, and 175 ns for the ν_0, ν_1, and ν_2 transitions, respectively. These represent the transit times of Ps atoms traveling at 7×10^6 cm/s through each waveguide. The inhomogeneous microwave field distribution in the single transverse mode in the waveguide with which the atoms interacted in the experiments was described by a sinusoidal function with a period of $2T_{\rm int}$. The finite atom-field interaction time represented by this function, combined with the natural spectral width of the $2\,^3S_1 \rightarrow 2\,^3P_J$ transitions, accounted for in the calculations by the finite spontaneous emission rate of the $2\,^3P_J$ levels, yielded spectral features with 60 MHz FWHM as observed in the experiments. The amplitude of the microwave field in the waveguides in the experiments was not precisely known. In the calculations, this was therefore set such that on resonance in each calculated spectrum, ~20% depopulation of the $1\,^3S_1$ level occurred. This was consistent with the conditions under which the experiments were performed with the output power from the microwave source set to ensure that the transitions probed were driven below saturation.

The effects of spontaneous emission in this four-level system, which preceded the ground-state annihilation that gave rise to the signal measured in the experiments, were accounted for through the collapse operators L_k in Eq. (7). For all calculations, only spontaneous emission from the $2\,^3P_J$ and $2\,^3P_{J'}$

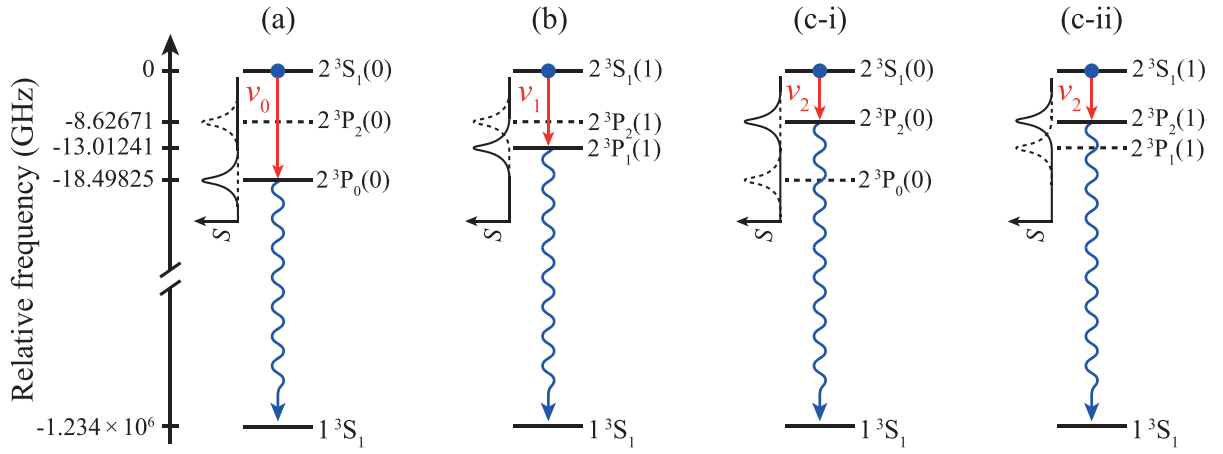

FIG. 10. Schematic diagram of the scenarios considered when calculating QI effects on (a) the $2\,^3S_1 \rightarrow 2\,^3P_0$, i.e., ν_0, (b) the $2\,^3S_1 \rightarrow 2\,^3P_1$, i.e., ν_1, and (c-i) and (c-ii) the $2\,^3S_1 \rightarrow 2\,^3P_2$, i.e., ν_2 transitions. The value of $|M_J|$ of the sublevels in each case is indicated in brackets.

levels to the $1\,^3S_1$ ground level was considered. This occurred at a rate of $1/\tau_{2P}$, where $\tau_{2P} = 3.19$ ns.

The energy level structure accounted for in the calculation of the ν_0, ν_1, and ν_2 spectral line shapes is depicted schematically in Fig. 10. For all calculations, the excited-state population was initially set to reside in a pure state, i.e., one $2\,^3S_1$ sublevel with a selected value of M_J denoted $2\,^3S_1(M_J)$ in Table IV and Fig. 10. The set of basis states considered when calculating each spectral profile included this one particular $2\,^3S_1(M_J)$ sublevel, and all $2\,^3P_J(M_J)$ sublevels to which $\Delta M_J = 0$ electric dipole transitions were allowed.

To calculate the spectral profile associated with the $2\,^3S_1 \rightarrow 2\,^3P_0$ transition at the frequency $\omega_0 = 2\pi\,\nu_0 = 2\pi \times 18.498\,25$ GHz, two ^3P sublevels were considered in addition to the initial $2\,^3S_1$ level and the $1\,^3S_1$ ground level as shown in Fig. 10(a). These were the resonant $2\,^3P_0$ sublevel with $M_J = 0$, i.e., the $2\,^3P_0(0)$ sublevel, and the off-resonant $2\,^3P_0(0)$ sublevel. The restrictions imposed by the selection rules for electric dipole transitions meant that the $2\,^3S_1(0) \rightarrow 2\,^3P_2(0)$ transition is the only $\Delta M_J = 0$ electric dipole transition within the $n = 2$ fine structure that can cause QI on the ν_0 resonance.

The calculated spectral line shape was obtained by evaluating the change in the population of the $1\,^3S_1$ ground level following the interaction with the microwave field as the frequency of this field was tuned through resonance. The result of this calculation is displayed as the continuous gray curve in Fig. 11(a). Lorentzian and Fano functions were fit to this calculated line shape to elucidate any QI shifts of the line center from the theoretically predicted resonance frequencies initially input into the calculations. From the results of this fitting procedure, it can be concluded that this calculated spectral profile is not asymmetric, i.e., $q > 10^6$. As a result, the process of fitting the Lorentzian and Fano functions to the calculated line shapes both yielded the same centroid frequencies. The centroid of the calculated spectral profile is, however, slightly shifted from the interval between the $2\,^3S_1$ and $2\,^3P_0$ levels input into the calculations. This shift of $-2\pi \times 156$ kHz is an effect of QI with the off-resonant transition to the $2\,^3P_2$ level. The magnitude of this shift is

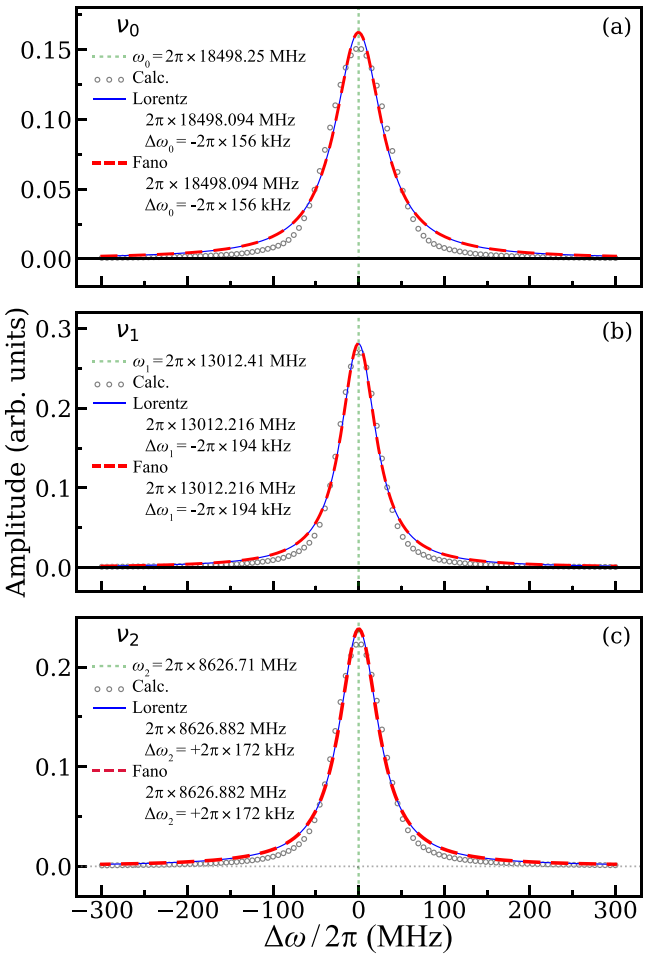

FIG. 11. Calculated line shapes showing the shift in the resonance frequency arising from the presence of far-detuned off-resonance transitions. The line shapes are fitted with Lorentz and Fano functions. Both functions yield identical results because of the lack of asymmetry. The ν_0 and ν_1 resonances are pulled by the ν_2 resonance yielding a negative frequency shift as shown in (a) and (b). The ν_2 resonance (c) is shifted positively. The width of the line shapes is ≈60 MHz.

comparable to that estimated for two interfering transitions of equal spectral intensity, i.e., $\Delta\nu \simeq \Gamma_m^2/2\Delta = 183$ kHz, where $\Delta = 18.498\,25$–$8.626\,71$ GHz and $\Gamma_m = 60$ MHz. The deviation of the calculated line shapes from the best-fit Lorentzian function arises because of the finite interaction time with the inhomogeneous microwave field accounted for in the calculations.

In the case of the $2\,^3S_1 \rightarrow 2\,^3P_1$ transition at frequency $\omega_1 = 2\pi\,\nu_1 = 2\pi \times 13.012\,41$ GHz, the ^3P sublevels considered in the calculation were the near-resonant $2\,^3P_1(1)$ sublevel and the off-resonant $2\,^3P_2(1)$ sublevel, as indicated in Fig. 10(b). Fitting Lorentzian and Fano functions to the calculated spectra displayed in Fig. 11 again yielded equal centroid transition frequencies. These were shifted by $-2\pi \times 194$ kHz from the value input into the calculations because of the effects of QI. The q value in excess of 10^6, obtained by fitting the Fano function, indicated that the calculated spectral profile was not asymmetric.

Finally, for the $2\,^3S_1 \rightarrow 2\,^3P_2$ transition at frequency $\omega_2 = 2\pi\,\nu_2 = 2\pi \times 8.626\,71$ GHz, the calculations were performed for sublevels with $M_J = 0$ and 1 since allowed electric dipole transitions can occur between these levels for both of these values of M_J. For $M_J = 0$, the sublevels included in the calculations were the near-resonant $2\,^3P_2(0)$ sublevel and the off-resonant $2\,^3P_0(0)$ sublevel, as indicated in Fig. 10(c-i). For $M_J = 1$, the sublevels included in the calculations were the near-resonant $2\,^3P_2(1)$ sublevel and the off-resonant $2\,^3P_1(1)$ sublevel, as indicated in Fig. 10(c-ii). Fitting the results of these calculations in Fig. 11 to Lorentzian and Fano line-shape functions yielded centroid transition frequencies shifted by $+2\pi \times 172$ kHz from the value input into the calculation, and again there is no indication of any asymmetry.

These results suggest that the frequency shifts and asymmetries observed in the measured spectral profiles do not result directly from effects of QI involving the strong $\Delta M_J = 0$ electric dipole transitions between the triplet $n = 2$ levels. Additional test calculations performed with atoms initially prepared in a superposition of the $2\,^3S_1(0)$ and $2\,^3S_1(1)$ sublevels, and including effects of QI arising from weak coupling to the $2\,^1P_1$ level that could occur in the magnetic fields employed in the experiments, did not yield enhanced frequency shifts or asymmetries.

VI. EVALUATION OF SYSTEMATIC EFFECTS

A. Doppler effects

Due to the low mass of Ps, even atoms with thermal energies (i.e., on the order 40 meV) have large speeds, which results in significant Doppler broadening of $1\,^3S_1 \rightarrow 2\,^3P_J$ line shapes (see Fig. 12). To determine the Doppler spread (i.e., the velocity spread) of Ps atoms emitted from the silica target, the $1\,^3S_1 \rightarrow 2\,^3P_J$ transition was measured as a function of the UV laser wavelength. As the laser light propagated along the x direction, only the x velocity distribution was measured. However, the pore structures of the silica samples are randomly orientated [64], and the Ps velocity distributions in the x and y directions are expected to be identical. Since the microwave radiation also propagates along the x direction, any difference between the x and y Ps velocity distributions will not affect the measurements; unexpected variations in the y distribution, which has not been directly measured, may affect the background signal, but the signal parameter S_γ is not sensitive to this.

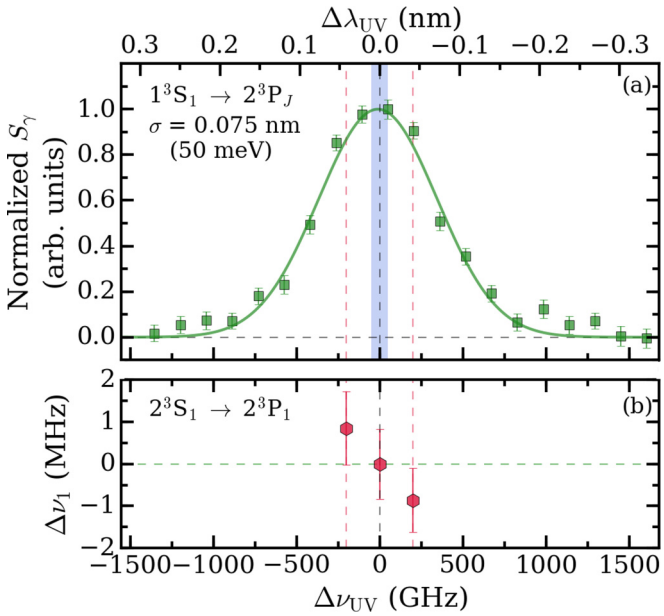

FIG. 12. (a) An example of a Doppler-broadened line shape of the $1\,^3S_1 \rightarrow 2\,^3P_J$ transition centered around 243 nm, where the natural linewidth is ≈50 MHz, but the observed linewidth is ≈900 GHz. (b) Relative shift in the $2\,^3S_1 \rightarrow 2\,^3P_1$ transition as a function of UV detuning. The dashed vertical lines in (a) indicate the UV laser wavelengths used for the measurements shown in (b), and the shaded bar indicates the 100 GHz bandwidth of the UV laser.

An example of a Doppler profile is shown in Fig. 12(a). It can be seen that, due to the large transverse velocity spread of the Ps atoms, the observed spectral width is much broader than the 50 MHz natural width. This $1\,^3S_1 \rightarrow 2\,^3P_J$ line shape was fitted with a Gaussian function, which yielded a Doppler width of ≈900 GHz FWHM. This Doppler profile represents the full velocity distribution (v_x) of the ground-state atoms in the direction of propagation of the UV laser light. The rms transverse speed of the Ps atoms is calculated from the width of the Doppler profile as $v_x^{\rm rms} = \sigma c/\lambda_{UV} \approx 9.3 \times 10^6$ cm/s. When the UV laser was tuned to the resonance wavelength ($\lambda_{UV} = 243.01$ nm) to drive the $2\,^3S'_1$ transition, the 100 GHz bandwidth of the laser only selected atoms with speeds $|v_x|$ below 10^6 cm/s. With the laser on resonance (and properly aligned), the transverse angular distribution after laser selection will be symmetric: therefore, the laser-induced transverse Ps velocity selection results in Doppler *broadening* of the ν_J line shapes of <3 MHz.

Although the velocity selection due to the UV excitation laser bandwidth is centered on the $v_x = 0$ atoms, the excited state v_x distribution will be shifted by the recoil associated with photon absorption. This shift has magnitude $v_{\rm recoil} = h/2m_e\lambda_{UV} \approx 1.5 \times 10^5$ cm/s. The resulting Doppler shifts ($\Delta\nu_J = \nu_J \times v_{\rm recoil}/c$) are −93, −65, and −43 kHz for the ν_0, ν_1, and ν_2 transitions, respectively. This effect can be controlled by appropriate detuning, or retroreflecting, the excitation laser light. The recoil shifts have been added as

systematic errors since these controls were not applied in the present work. We note also that this was not taken into account in Ref. [18].

Doppler shifts may also arise from a misalignment of the laser relative to the waveguide axis. This would lead to the production of excited-state atoms with an asymmetric speed distribution relative to the waveguide axis. That is, on average, Ps atoms could be moving toward or away from the direction of propagation of the microwave radiation. By measuring the position of the laser relative to the windows on either side of the vacuum chamber, we estimate that the laser was aligned to the waveguide axis to within $\pm$ 2°. The resulting Doppler shifts $[\nu_J \times v_z \sin(\theta)/c]$ from a $\pm$ 2° misalignment are $\pm$215, $\pm$150, and $\pm$100 kHz for the ν_0, ν_1, and ν_2 transitions, respectively.

Figure 12(b) shows the ν_1 transition frequencies measured when the UV laser was detuned away from the $\lambda_{UV} =$ 243.01 nm resonance wavelength by $\pm$200 GHz. This had a similar effect to that of laser-waveguide misalignment, i.e., generating $2\,^3S_1$ atoms that were, on average, traveling either toward or away from the direction of propagation of the microwave radiation. Because the UV laser and microwave radiation were propagating in opposite directions, as shown in Fig. 2(b), the shift in the ν_1 transition was expected to be $\Delta\nu_1 = \nu_1 \Delta\nu_{UV}/\nu_{UV} = \pm 2$ MHz for $\Delta\nu_{UV} = \mp 200$ GHz detuning, although this will be reduced if slower atoms in the distribution are preferentially excited by the microwave radiation. These data verify that microwave transitions were not subject to any significant Doppler shifts caused by an incorrect UV laser wavelength, not including the recoil shift mentioned above.

Second-order Doppler shifts are negligible in the current experiment, with values of $\nu_J \times (v_z^{rms}/2c)^2 \approx 0.5$, 0.4, and 0.3 kHz for the ν_0, ν_1, and ν_2 transitions, respectively.

B. Motional Stark effects

Ps atoms that are not moving parallel to a magnetic field can experience an induced motional electric field, with concomitant Stark shifts [65]. Although the UV laser selected atoms with small transverse speeds in the x direction, the excited atoms had a broader distribution of speeds in the y direction (see Fig. 2). In the most extreme case, for atoms moving with speed 10^7 cm/s perpendicular to a 100 G magnetic field, the induced motional electric field ($\vec{F} = \vec{v} \times \vec{B}$) is 10 V/cm. In reality, most of the atoms had lower transverse speeds, and they were not traveling perpendicular to the magnetic field, and the actual motional electric field in the experiment was much lower. The angular distribution of Ps atoms emitted from SiO_2 targets can be reasonably well described by a cosine distribution [66], and the average angle, in the y direction, of emission from the SiO_2 target is estimated to be $\theta_{avg} \approx 27°$. The motional electric field due to atoms traveling with speed $v_y^{rms} = 10^7$ cm/s at θ_{avg} will then be $\approx$4 V/cm, which will cause a motional Stark shift of $\approx +130$ kHz. However, the induced motional electric field is perpendicular to and linear in B, and the Stark shift depends on B^2. Thus, any such shift will extrapolate to zero along with the Zeeman shifts (see Fig. 7), and therefore will not contribute to the systematic error of the measurements.

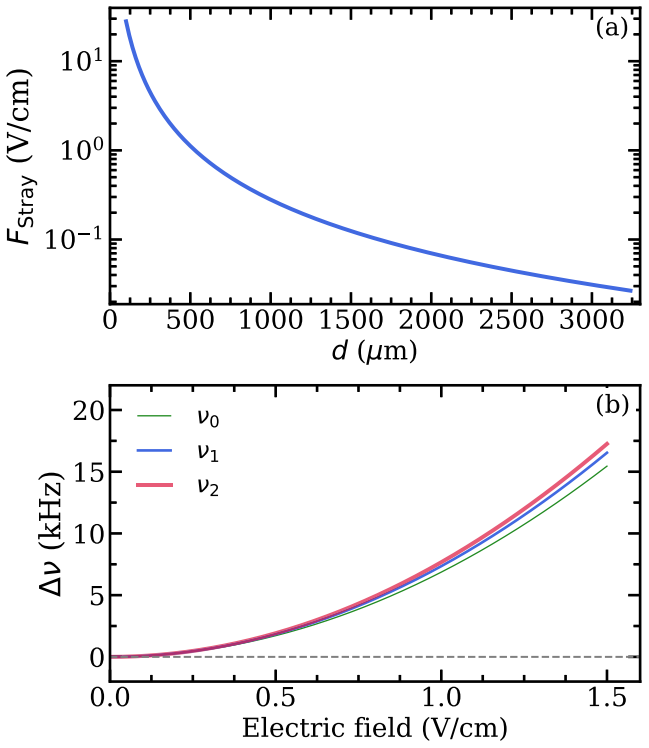

FIG. 13. (a) Estimated magnitude of stray electric fields in the waveguides as a function of distance from the grids. (b) Stark shift of the ν_J transitions as a function of electric field.

C. Stray electric fields

The waveguides used in this work were constructed from an aluminum plate and a tungsten mesh, and it is possible for these materials to support patch potentials, giving rise to stray electric fields. Such fields are ubiquitous and cannot easily be eliminated, even on atomically clean surfaces. Such potentials have been extensively studied (e.g., [67–69]), and they are typically found to be on the order of 100 mV for a wide range of materials.

Highly excited (Rydberg) atoms are extremely sensitive to electric fields [70], and they can therefore be used to probe very weak stray electric fields [71]. Based on previous studies using Rydberg atoms [72], we estimate the stray electric fields in the waveguides to be no larger than $F_{stray} \approx 3 \times 10^{-5}/d^2$ V/m. The corresponding stray field strength as a function of d, the distance from the waveguide surface, is shown in Fig. 13(a). The fields at a distance of $d = 100$ μm from the grids is $\approx$30 V/cm. At the center of the WR-51 guide, $d = 3.25$ mm, the fields are estimated to be only 28 mV/cm. The average stray field across the WR-51 guide is calculated to be 0.91 V/cm, which equates to a Stark shift of +5.9, +6.3, and +6.5 kHz in the ν_0, ν_1, and ν_2 transitions, respectively, as shown in Fig. 13(b). Since the WR-51 waveguide is the narrowest used (see Table II), the Stark shift of all the ν_J transitions due to stray fields is therefore conservatively estimated to be less than +7 kHz.

TABLE V. List of estimated systematic uncertainties as described in the text.

Contribution	σ_{sys} (kHz)		
	ν_0	ν_1	ν_2
Laser misalignment	±215	±150	±100
Recoil Doppler	−93	−65	−43
Second-order Doppler	+ 0.5	+ 0.4	+0.3
Stray electric fields	<+7	<+7	<+7
ac Stark	<+7	<+7	<+7
Total	±323	±229	±157

D. ac Stark shifts

High powers of microwave radiation can induce ac Stark shifts [36], which, if present, would also be expected to result in line broadening, as shown in Fig. 6. For $P_{input} \approx 25$ mW, the linewidth was determined to be 90 MHz, and the microwave-induced signal, S_γ, appeared to have saturated, and therefore we assumed this microwave power as the saturation intensity. For 20% of this saturation intensity, $P_{input} \approx 5$ mW, the linewidths were ≈60 MHz, slightly wider than the natural linewidth (50 MHz), and they were observed to be independent of power below 12 mW input. The microwave field strength at 5 mW was calculated to be 4.1 V/cm, which would result in an ac Stark shift of +6.88 kHz. The microwave radiation powers used in all three measurements were similar, and the induced ac Stark shift uncertainty was estimated to be <+7 kHz for all transitions.

E. Total systematic errors

The error budget for all systematic effects σ_{sys} is summarized in Table V, and they are clearly dominated by Doppler shifts due to possible laser misalignment. We neglect the fact that all effects other than the laser alignment lead to shifts in only one direction, and we have not added the errors in quadrature to account for possible correlations. These estimates, therefore, constitute a conservative estimate of the total systematic errors.

VII. NEW PHYSICS

Given that Ps is almost entirely described by QED [2,3], it is tempting to attribute the apparent disagreement with QED theory to some sort of process not included in the Standard Model, generically known as new physics (NP) [4]. The asymmetric line shapes observed for the ν_1 and ν_2 transitions preclude any such attribution, since it is not possible to determine the actual transition frequencies, or, therefore, if there is in fact any disagreement with theory. As discussed above, the ν_0 transition does exhibit a symmetric line shape, and we interpret the measured line center as the resonance frequency of the transition, at least to the extent allowed by the quantum interference effects discussed in Sec. V. Then, the experimentally determined transition frequency shows a deviation of 2.77 MHz with respect to the theoretical QED prediction. In principle, this deviation may be related to the existence of a new force, beyond the Standard Model of particle physics. Such forces could appear in two flavors, depending on the nature of the mediator of the interaction. Scalar and vector mediators lead to a spin-independent force, whereas the exchange of pseudoscalars or axion-like particles (ALPs) would give rise to spin-dependent interactions [73].

Let us assume that a novel force between electrons and positrons emerges as a consequence of exchanging a scalar boson of mass m_ϕ. Then the leptons within a Ps atom would experience an interaction potential given by

$$V(r) = \frac{g_e^2}{4\pi}\frac{e^{-rm_\phi}}{r}, \tag{9}$$

where g_e is the dimensionless coupling constant of the mediator with the leptons. This interaction induces a shift of the atomic energy levels that depends on the mass of the mediator and the coupling strength. Therefore, for a particular shift, ΔE, of Ps energy levels (in general the maximum between the experimental and theoretical uncertainties [73], although here it is relative to QED predictions), it is possible to constrain the coupling constant as a function of the mass of the mediator. In particular, for the $2\,^3S_1 \to 2\,^3P_0$ transition ($2S \to 2P$, since the spin state is irrelevant for this interaction force), the energy shift is given by

$$\Delta E = \langle\psi_{2S}|V(r)|\psi_{2S}\rangle - \langle\psi_{2P}|V(r)|\psi_{2P}\rangle, \tag{10}$$

where $|\psi_{2S}\rangle$ and $|\psi_{2P}\rangle$ refer to the wave functions of the $2S$ and $2P$ states in Ps, respectively. The results of this analysis performed for the observed 2.77 MHz shift in the $2\,^3S_1 \to 2\,^3P_0$ transition are shown in Fig. 14. It is evident from the figure that for the relevant mass range for atomic systems, the coupling constant compatible with our measurement is already ruled out by previous spectroscopic studies in Ps [74], and, more stringently, by measurements of the gyromagnetic factor of the electron [75].

The $2\,^3S_1 \to 2\,^3P_0$ transition may also be affected by spin-dependent forces, in which case the interaction potential is given by

$$V(r) = \frac{-g_e^2}{12\pi m_e^2}\left[\boldsymbol{S}_1\cdot\boldsymbol{S}_2\left(4\pi\delta^3(\mathbf{r}) - \frac{m_{ALP}^2 e^{-rm_{ALP}}}{r}\right) - \frac{S_{12}(\hat{r})}{4}\left(\frac{m_{ALP}^2}{r} + \frac{3m_{ALP}}{r^2} + \frac{3}{r^3}\right)e^{-rm_{ALP}}\right], \tag{11}$$

where $\boldsymbol{S}_i$ is the spin operator of the ith lepton, m_{ALP} is the mass of the mediator, and

$$S_{12}(\hat{r}) = 4[3(\boldsymbol{S}_1\cdot\hat{r})(\boldsymbol{S}_2\cdot\hat{r}) - \boldsymbol{S}_1\cdot\boldsymbol{S}_2], \tag{12}$$

which only affects electronic states with $\ell \neq 0$. The corresponding constraints on a pseudoscalar mediator phase space, determined using Eq. (11), are shown in Fig. 15. As in the case of a scalar mediator, the observed 2.77 MHz discrepancy between QED and our experimental data is already entirely ruled out by previous measurements and astrophysical bounds.

The existence of pseudoscalars would induce a state-dependent shift of Ps energy levels; triplet states are shifted to lower energies (except states with $J = 1$), whereas singlet states show an energy displacement toward higher energies. Thus, the sign of the induced energy shift depends on the spin state, as anticipated in Eq. (11), whereas its magnitude

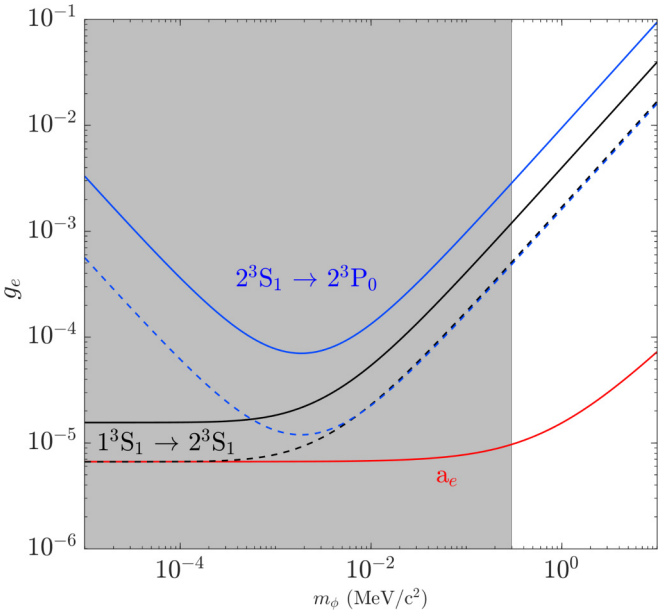

FIG. 14. Constrained parameter space for a scalar mediator [73]. The solid blue curve denotes the lower bound for a shift of 2.77 MHz for the $2S \rightarrow 2P$ transition. The solid black curve is the same observable obtained for a measurement of the Ps $1S \rightarrow 2S$ interval [74]. The dashed curves represent the constraints that would be obtained if the corresponding measurements were performed with uncertainties equal to the current QED uncertainties [73]. The red curve is the bound obtained from measurements of the electron gyromagnetic factor, a_e [75]. The shaded gray region represents the parameter space constrained by astrophysical observations [76].

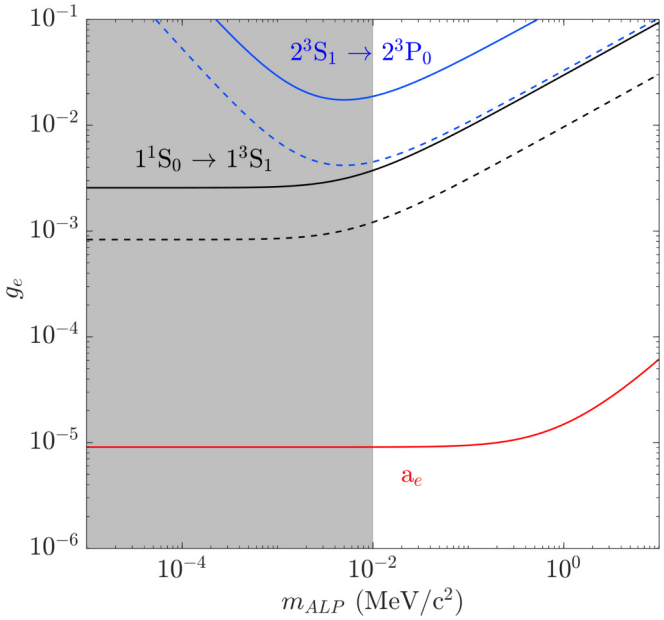

FIG. 15. Constrained parameter space for a pseudoscalar mediator [73]. The solid blue curve denotes the lower bound for a shift of 2.77 MHz for the $2\,^3S_1 \rightarrow 2\,^3P_0$ transition. The solid black curve is the same observable obtained for a measurement of the Ps $1\,^1S_0 \rightarrow 1\,^3S_1$ transition [77–79]. The dashed curves represent the constraints that would be obtained if the corresponding measurements were performed with uncertainties equal to the current QED uncertainties [73]. The red curve is the bound obtained from measurements of the electron gyromagnetic factor, a_e [75]. The shaded gray region represents the parameter space constrained by astrophysical observations [76].

correlates with the state's electronic nature; P states have a null probability of finding the leptons at the same point in space, leading to a small energy shift. However, S states exhibit some overlap near the origin, thus activating the Dirac δ function in Eq. (11) and leading to larger energy shifts. More precise measurements may be able to probe such effects, but only if the mechanism(s) behind the observed asymmetries and shifts are fully understood or eliminated.

The realm of physics beyond the Standard Model offers more exotic scenarios through which novel fields or particles could give rise to shifts of Ps energy levels. One example is the chameleon model, in which a new scalar interacts with the leptons in a manner that depends on the density of the environment [80]. Although this model offers a mechanism to avoid some astrophysical constraints, the associated parameter space has already been constrained by high-precision atomic spectroscopy [81].

Another example is the Arkani-Hamed–Dimopoulos–Dvali (ADD) model [82], in which it is assumed that gravity operates in a (compactified) higher-dimensional space, whereas the rest of the fundamental forces exist only in a four-dimensional membrane embedded in this space. This makes gravity much weaker than all other forces as experienced on a macroscopic scale, but at short range the existence of the higher-dimensional space may give rise to a gravitational potential that is strong enough to affect atomic and molecular energy levels [83]. This model has been constrained by high-precision spectroscopy in molecular ions [84], and is therefore also unlikely to explain our observations. Thus, while a more exotic NP-type of explanation cannot be ruled out, it would likely require some unusual features in order to explain our observations without conflicting with other measurements or astrophysical bounds.

VIII. DISCUSSION AND CONCLUSIONS

The frequencies of the ν_0, ν_1, and ν_2 transitions obtained using both Lorentzian and Fano functions to fit the measured line shapes are summarized in Table VI. For the ν_0 case, the line shape was found to be highly symmetric (see Fig. 9), and the Lorentzian and Fano profiles give the same frequency. This is not the case for the asymmetric ν_1 and ν_2 line shapes, which yield significantly different frequencies, neither of which can be expected to correspond to the true resonance frequency.

The present data are compared with all prior measurements in Fig. 16. Also shown in this figure are the zero-field extrapolated frequencies obtained for the ν_1 and ν_2 transitions by finding the maximum (peak) value of the Fano fits [44]. These frequencies are closer to the theory values, and the agreement is almost exact for the ν_2 case. As discussed above, the Fano resonance frequency ν_R does not correspond to the resonance frequency since it depends explicitly on the q value, which is in this case simply an empirical metric of the line-shape asymmetry. The peak position is also not expected to directly correspond to the resonance frequency, but it may be

TABLE VI. Comparison of the results from current measurements (using both Lorentz and Fano fits) and theoretical calculations of the Ps $n = 2$ fine-structure intervals. The last two columns indicate the discrepancy between theory and measurements obtained using the Lorentz and Fano profiles. The theoretical values are from Ref. [15].

Transition	Theory (MHz)	Exp: Lorentz (MHz)	Exp: Fano (MHz)	$\Delta\nu_L$ (MHz)	$\Delta\nu_F$ (MHz)
ν_0	$18\,498.25 \pm 0.08$	$18\,501.02 \pm 0.57_{stat} \pm 0.323_{sys}$	$18\,501.09 \pm 0.62_{stat} \pm 0.323_{sys}$	+2.77	+ 2.84
ν_1	$13\,012.41 \pm 0.08$	$13\,008.41 \pm 0.52_{stat} \pm 0.229_{sys}$	$13\,014.13 \pm 0.58_{stat} \pm 0.229_{sys}$	−4	+1.72
ν_2	8626.71 ± 0.08	$8628.28 \pm 0.35_{stat} \pm 0.157_{sys}$	$8624.68 \pm 0.35_{stat} \pm 0.157_{sys}$	+1.57	−2.03

closer than the Lorentzian maxima since fitting the symmetric Lorentzian function to asymmetric data introduces errors in the inferred peak position (exacerbated by the fact that the line is relatively broad). However, this approach does not account for the underlying physics that gives rise to the asymmetry, and while it may provide a better approximation, it is clearly not suitable for precision measurements.

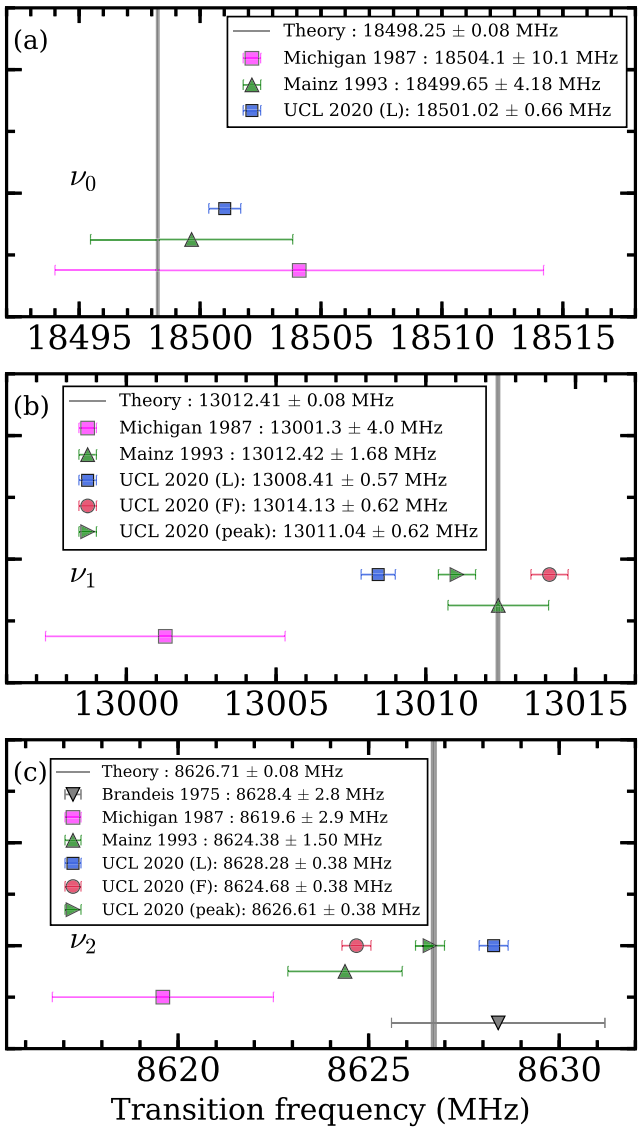

FIG. 16. Comparison of the previous and present measurements with theory for the (a) ν_0, (b) ν_1, and (c) ν_2 transitions. Results from Lorentz (L) and Fano (F) line profile fits are shown for the current measurements of ν_1 and ν_2 intervals. Also shown for these transitions are the maximum (peak) values obtained from the Fano profiles, as discussed in the text. The theoretical values with uncertainties are indicated by the vertical solid lines. Statistical and systematic uncertainties for the experimental data have been added in quadrature.

To extract the true resonance frequencies from the asymmetric line shapes, it will be necessary to perform more sophisticated line-shape modeling. The calculations already performed indicate that the QI effects considered in Sec. V are not responsible for our observations. However, the possibility that other more subtle interference effects exist that can give rise to unexpectedly large asymmetries or shifts will have to be investigated in more detail.

There are several improvements that can be made to the experimental methodology: One important improvement is the elimination of the axial magnetic field. This can be achieved by extracting the positron beam from the magnetic field using electrostatic lenses [85,86], and it will reduce Zeeman shifts to negligible levels. Moreover, it would remove the need to perform measurements at many different fields, which would considerably reduce the statistical uncertainty (for the same sized dataset).

Alternative $2\,^3S_1$ production methods are possible; a two-photon Doppler-free excitation process [87] would increase the production efficiency by a factor of ≈5 [37]. However, this method does not provide any velocity selection, so not all of the additional excited atoms would contribute to the signal. Excitation to $3\,^3P_J$ levels, followed by stimulated emission to the $2\,^3S_1$ level [88], could offer an increase in the production efficiency of ≈30%.

The count rate could be improved with increased detector coverage, either by using larger scintillators or adding more γ-ray detectors. Alternatively, if the $2\,^3S_1$ atoms were directly detected using a microchannel plate detector, we estimate that it would be possible to obtain an order of magnitude increase in the count rate.

In general, atoms in highly excited Rydberg states [70] are extremely sensitive to electric and magnetic fields, and they can therefore be utilized as field probes [71]. Future experiments will employ microwave spectroscopy of a Rydberg He beam to probe and characterize the stray fields in the microwave guide [31] by studying Stark and Zeeman effects on the fine structure of He Rydberg states [89].

Currently, the largest source of systematic uncertainty in our measurements is the Doppler effect from possible laser misalignment. To characterize this effect, a second microwave antenna can be added to the waveguide, so that measurements with microwave radiation propagating in either direction (i.e., $+x$ or $-x$) can be taken [17]. This will allow any laser misalignment to be corrected.

Perhaps the most significant improvement to the experimental methodology would be to perform measurements

using the separated oscillatory field (SOF) method of Ramsay [90,91]. One of the main limitations of the measurements described here was the 50 MHz natural linewidth; finding the center frequency with a precision more than 1000 times smaller than the linewidth is challenging even without asymmetric line shapes. The Ramsay SOF approach allows transitions to be observed with experimental linewidths that are narrower than the natural width, and it does not require explicit knowledge of the exact line shape; instead of scanning the frequency over a resonance, an interference signal is measured as a function of the phase difference between two different excitation fields, and the resonance frequency is determined from the frequency dependence of the phase difference at which this signal is maximal.

A recently developed variation of the SOF method is the frequency offset separated oscillatory field (FOSOF) technique [92]. This causes a temporal oscillation of the SOF signal at the offset frequency, from which the resonance frequency can be extracted. This method is not sensitive to the frequency response of the system, and it has a simple line shape, offering much improved precision and the ability to change, and hence characterize and control, systematic effects. QI effects are still observed using SOF or FOSOF methods, since they are intrinsic to the excitation process, but they are smaller because the effective linewidths are narrower. Although there are considerable technical challenges to be overcome, a FOSOF measurement performed using Ps is feasible, and would represent a significant advance in Ps spectroscopy.

We have observed asymmetric line shapes for the ν_1 and ν_2 transitions in Ps, and an apparent shift of the symmetric ν_0 transition. The most obvious QI and NP mechanisms, as considered above, cannot explain these observations. Experimental artifacts also seem unlikely in light of the qualitatively different line shapes observed in the three different transitions. Taken together, the relative distortions of these line shapes imply that it is the atomic structure of Ps that is driving the underlying mechanism(s) responsible for our observations. Whether this occurs via some subtle QI mechanism, an unexpected coupling between states, or some sort of exotic NP remains to be seen. Certainly, further experiments and more theoretical work are needed.

ACKNOWLEDGMENTS

We gratefully acknowledge L. Liszkay for providing silica samples, G. S. Adkins, G. Gribakin, A. P. Mills, Jr., and E. A. Hessels for helpful discussions, A. Matveev for pointing out the recoil Doppler shifts, R. Jawad, A. Morgan, and J. Dumper for technical assistance, and R. E. Sheldon and A. M. Alonso for contributions to the preliminary stages of this research. This work was funded by the EPSRC under Grant No. EP/R006474/1.

[1] J. A. Wheeler, Polyelectrons, Ann. N.Y. Acad. Sci. **48**, 219 (1946).
[2] W. Bernreuther and O. Nachtmann, Weak interaction effects in positronium, Z. Phys. C **11**, 235 (1981).
[3] S. G Karshenboim, Precision study of positronium: Testing bound state QED theory, Int. J. Mod. Phys. A **19**, 3879 (2004).
[4] M. S. Safronova, D. Budker, D. DeMille, D. F. J. Kimball, A. Derevianko, and C. W. Clark, Search for new physics with atoms and molecules, Rev. Mod. Phys. **90**, 025008 (2018).
[5] H. A. Bethe and E. E. Salpeter, *Quantum Mechanics of One- and Two-Electron Atoms* (Springer, Berlin, 1957).
[6] S. G. Karshenboim, Precision physics of simple atoms: QED tests, nuclear structure and fundamental constants, Phys. Rep. **422**, 1 (2005).
[7] S. R. Lundeen, Fast beam measurement of hydrogen fine structure, in *Atomic Masses and Fundamental Constants 5*, edited by J. H. Sanders and A. H. Wapstra (Springer US, Boston, 1976), pp. 571–577.
[8] A. M. Alonso, B. S. Cooper, A. Deller, S. D. Hogan, and D. B. Cassidy, Controlling Positronium Annihilation with Electric Fields, Phys. Rev. Lett. **115**, 183401 (2015).
[9] A. I. Alekseev, Two-photon annihilation of positronium in the P-state, Sov. Phys. JETP **7**, 826 (1958).
[10] A. I. Alekseev, Three-photon annihilation of positronium in the P-state, Sov. Phys. JETP **9**, 1312 (1959).
[11] G. Breit and E. Teller, Metastability of hydrogen and helium levels, Astrophys. J. **91**, 215 (1940).
[12] A. H. Al-Ramadhan and D. W. Gidley, New Precision Measurement of the Decay Rate of Singlet Positronium, Phys. Rev. Lett. **72**, 1632 (1994).
[13] R. S. Vallery, P. W. Zitzewitz, and D. W. Gidley, Resolution of the Orthopositronium-Lifetime Puzzle, Phys. Rev. Lett. **90**, 203402 (2003).
[14] O. Jinnouchi, S. Asai, and T. Kobayashi, Precision measurement of orthopositronium decay rate using SiO_2 powder, Phys. Lett. B **572**, 117 (2003).
[15] A. Czarnecki, K. Melnikov, and A. Yelkhovsky, Positronium S-state spectrum: Analytic results at $o(m\alpha^6)$, Phys. Rev. A **59**, 4316 (1999).
[16] R. S. Conti, S. Hatamian, L. Lapidus, A. Rich, and M. Skalsey, Search for C-violating, P-conserving interactions and observation of $2\ ^3S_1$ to $2\ ^1P_1$ transitions in positronium, Phys. Lett. A **177**, 43 (1993).
[17] D. Hagena, R. Ley, D. Weil, G. Werth, W. Arnold, and H. Schneider, Precise Measurement of $n = 2$ Positronium Fine-Structure Intervals, Phys. Rev. Lett. **71**, 2887 (1993).
[18] L. Gurung, T. J. Babij, S. D. Hogan, and D. B. Cassidy, Precision Microwave Spectroscopy of the Positronium $n = 2$ Fine Structure, Phys. Rev. Lett. **125**, 073002 (2020).
[19] K. Pachucki and S. G. Karshenboim, Complete Results for Positronium Energy Levels at Order $m\alpha^6$, Phys. Rev. Lett. **80**, 2101 (1998).
[20] G. S. Adkins, R. N. Fell, and J. Sapirstein, Two-loop correction to the orthopositronium decay rate, Ann. Phys. **295**, 136 (2002).
[21] J. Zatorski, $o(m\alpha^6)$ corrections to energy levels of positronium with nonvanishing orbital angular momentum, Phys. Rev. A **78**, 032103 (2008).
[22] K. Pachucki and S. G. Karshenboim, Higher-order recoil corrections to energy levels of two-body systems, Phys. Rev. A **60**, 2792 (1999).

[23] B. A. Kniehl and A. A. Penin, Order $\alpha^7 \ln(1/\alpha)$ Contribution to Positronium Hyperfine Splitting, Phys. Rev. Lett. **85**, 5094 (2000).

[24] M. Baker, P. Marquard, A. A. Penin, J. Piclum, and M. Steinhauser, Hyperfine Splitting in Positronium to $\mathcal{O}(\alpha^7 m_e)$: One Photon Annihilation Contribution, Phys. Rev. Lett. **112**, 120407 (2014).

[25] G. S. Adkins, M. Kim, C. Parsons, and R. N. Fell, Three-Photon-Annihilation Contributions to Positronium Energies at Order $m\alpha^7$, Phys. Rev. Lett. **115**, 233401 (2015).

[26] G. S. Adkins, L. M. Tran, and R. Wang, Positronium energy levels at order $m\alpha^7$: Product contributions in the two-photon-annihilation channel, Phys. Rev. A **93**, 052511 (2016).

[27] A. P. Mills, Jr., S. Berko, and K. F. Canter, Fine-Structure Measurement in the First Excited State of Positronium, Phys. Rev. Lett. **34**, 1541 (1975).

[28] S. Hatamian, R. S. Conti, and A. Rich, Measurements of the $2\ ^3S_1$-$2\ ^3P_J$ ($J = 0, 1, 2$) Fine-Structure Splittings in Positronium, Phys. Rev. Lett. **58**, 1833 (1987).

[29] B. S. Cooper, A. M. Alonso, A. Deller, T. E. Wall, and D. B. Cassidy, A trap-based pulsed positron beam optimised for positronium laser spectroscopy, Rev. Sci. Instrum. **86**, 103101 (2015).

[30] A. M. Alonso, B. S. Cooper, A. Deller, S. D. Hogan, and D. B. Cassidy, Positronium decay from $n = 2$ states in electric and magnetic fields, Phys. Rev. A **93**, 012506 (2016).

[31] D. B. Cassidy, Experimental progress in positronium laser physics, Eur. Phys. J. D **72**, 53 (2018).

[32] A. P. Mills, Jr. and E. M. Gullikson, Solid neon moderator for producing slow positrons, Appl. Phys. Lett. **49**, 1121 (1986).

[33] J. R. Danielson, D. H. E. Dubin, R. G. Greaves, and C. M. Surko, Plasma and trap-based techniques for science with positrons, Rev. Mod. Phys. **87**, 247 (2015).

[34] L. Liszkay, C. Corbel, P. Perez, P. Desgardin, M. F. Barthe, T. Ohdaira, R. Suzuki, P. Crivelli, U. Gendotti, A. Rubbia, M. Etienne, and A. Walcarius, Positronium reemission yield from mesostructured silica films, Appl. Phys. Lett. **92**, 063114 (2008).

[35] D. B. Cassidy, P. Crivelli, T. H. Hisakado, L. Liszkay, V. E. Meligne, P. Perez, H. W. K. Tom, and A. P. Mills, Jr., Positronium cooling in porous silica measured via Doppler spectroscopy, Phys. Rev. A **81**, 012715 (2010).

[36] W. Demtröder, *Laser Spectroscopy*, 3rd ed. (Springer, New York, 2003).

[37] A. M. Alonso, S. D. Hogan, and D. B. Cassidy, Production of $2\ ^3S_1$ positronium atoms by single-photon excitation in an electric field, Phys. Rev. A **95**, 033408 (2017).

[38] D. B. Cassidy, S. H. M. Deng, R. G. Greaves, and A. P. Mills, Jr., Accumulator for the production of intense positron pulses, Rev. Sci. Instrum. **77**, 073106 (2006).

[39] A. M. Alonso, B. S. Cooper, A. Deller, and D. B. Cassidy, Single-shot positron annihilation lifetime spectroscopy with LYSO scintillators, Nucl. Instrum. Methods Phys. Res., Sect. A **828**, 163 (2016).

[40] A. L. Stancik and E. B. Brauns, A simple asymmetric lineshape for fitting infrared absorption spectra, Vib. Spectrosc. **47**, 66 (2008).

[41] U. Fano, Effects of configuration interaction on intensities and phase shifts, Phys. Rev. **124**, 1866 (1961).

[42] A. R. P. Rau, Perspectives on the Fano resonance formula, Phys. Scr. **69**, C10 (2004).

[43] A. E. Miroshnichenko, S. Flach, and Y. S. Kivshar, Fano resonances in nanoscale structures, Rev. Mod. Phys. **82**, 2257 (2010).

[44] R. P. Brent, *Algorithms for Minimization Without Derivatives* (Dover, Mineola, NY, 2013).

[45] C. J. Foot, *Atomic Physics*, Oxford Master Series in Physics (Oxford University Press, Oxford, 2005).

[46] M. H. Rayment, L. Gurung, R. E. Sheldon, S. D. Hogan, and D. B. Cassidy, Multiring electrostatic guide for Rydberg positronium, Phys. Rev. A **100**, 013410 (2019).

[47] M. Horbatsch and E. A. Hessels, Shifts from a distant neighboring resonance, Phys. Rev. A **82**, 052519 (2010).

[48] C. J. Sansonetti, C. E. Simien, J. D. Gillaspy, J. N. Tan, S. M. Brewer, R. C. Brown, S. Wu, and J. V. Porto, Absolute Transition Frequencies and Quantum Interference in a Frequency Comb Based Measurement of the ^{6,7}Li D Lines, Phys. Rev. Lett. **107**, 023001 (2011).

[49] R. C. Brown, S. Wu, J. V. Porto, C. J. Sansonetti, C. E. Simien, S. M. Brewer, J. N. Tan, and J. D. Gillaspy, Quantum interference and light polarization effects in unresolvable atomic lines: Application to a precise measurement of the ^{6,7}Li D_2 lines, Phys. Rev. A **87**, 032504 (2013).

[50] D. C. Yost, A. Matveev, E. Peters, A. Beyer, T. W. Hänsch, and Th. Udem, Quantum interference in two-photon frequency-comb spectroscopy, Phys. Rev. A **90**, 012512 (2014).

[51] P. Amaro, B. Franke, J. J. Krauth, M. Diepold, F. Fratini, L. Safari, J. Machado, A. Antognini, F. Kottmann, P. Indelicato, R. Pohl, and José Paulo Santos, Quantum interference effects in laser spectroscopy of muonic hydrogen, deuterium, and helium-3, Phys. Rev. A **92**, 022514 (2015).

[52] A. Beyer, L. Maisenbacher, A. Matveev, R. Pohl, K. Khabarova, A. Grinin, T. Lamour, D. C. Yost, T. W. Hänsch, N. Kolachevsky, and T. Udem, The Rydberg constant and proton size from atomic hydrogen, Science **358**, 79 (2017).

[53] K. Kato, T. D. G. Skinner, and E. A. Hessels, Ultrahigh-Precision Measurement of the $n = 2$ Triplet P Fine Structure of Atomic Helium using Frequency-Offset Separated Oscillatory Fields, Phys. Rev. Lett. **121**, 143002 (2018).

[54] N. Bezginov, T. Valdez, M. Horbatsch, A. Marsman, A. C. Vutha, and E. A. Hessels, A measurement of the atomic hydrogen lamb shift and the proton charge radius, Science **365**, 1007 (2019).

[55] A. Marsman, M. Horbatsch, and E. A. Hessels, The effect of quantum-mechanical interference on precise measurements of the n = 2 triplet p fine structure of helium, J. Phys. Chem. Ref. Data **44**, 031207 (2015).

[56] A. Marsman, M. Horbatsch, and E. A. Hessels, Shifts due to neighboring resonances for microwave measurements of the $2\ ^3P$ fine structure of helium, Phys. Rev. A **86**, 012510 (2012).

[57] M. Horbatsch and E. A. Hessels, Shifts from a distant neighboring resonance for a four-level atom, Phys. Rev. A **84**, 032508 (2011).

[58] A. Marsman, E. A. Hessels, and M. Horbatsch, Shifts due to quantum-mechanical interference from distant neighboring resonances for saturated fluorescence spectroscopy of the 2^3S to 2^3P intervals of helium, Phys. Rev. A **89**, 043403 (2014).

[59] A. Marsman, M. Horbatsch, and E. A. Hessels, Interference between two resonant transitions with distinct initial and final

states connected by radiative decay, Phys. Rev. A **96**, 062111 (2017).

[60] T. Udem, L. Maisenbacher, A. Matveev, V. Andreev, A. Grinin, A. Beyer, N. Kolachevsky, R. Pohl, D. C. Yost, and T. W. Hänsch, Quantum interference line shifts of broad dipole-allowed transitions, Ann. Phys. **531**, 1900044 (2019).

[61] G. Lindblad, On the generators of quantum dynamical semigroups, Commun. Math. Phys. **48**, 119 (1976).

[62] V. Gorini, A. Kossakowski, and E. C. G. Sudarshan, Completely positive dynamical semigroups of N-level systems, J. Math. Phys. **17**, 821 (1976).

[63] J. R. Johansson, P. D. Nation, and F. Nori, QuTiP 2: A Python framework for the dynamics of open quantum systems, Comp. Phys. Commun. **184**, 1234 (2013).

[64] L. Liszkay, F. Guillemot, C. Corbel, J.-P. Boilot, T. Gacoin, E. Barthel, P. Pérez, M.-F. Barthe, P. Desgardin, P. Crivelli, U. Gendotti, and A. Rubbia, Positron annihilation in latex-templated macroporous silica films: Pore size and ortho-positronium escape, New J. Phys. **14**, 065009 (2012).

[65] S. M. Curry, Combined Zeeman and motional Stark effects in the first excited state of positronium, Phys. Rev. A **7**, 447 (1973).

[66] A. Deller, B. S. Cooper, T. E. Wall, and D. B. Cassidy, Positronium emission from mesoporous silica studied by laser-enhanced time-of-flight spectroscopy, New J. Phys. **17**, 043059 (2015).

[67] T. W. Darling, F. Rossi, G. I. Opat, and G. F. Moorhead, The fall of charged particles under gravity: A study of experimental problems, Rev. Mod. Phys. **64**, 237 (1992).

[68] A. Härter, A. Krükow, A. Brunner, and J. Hecker Denschlag, Long-term drifts of stray electric fields in a Paul trap, Appl. Phys. B **114**, 275 (2014).

[69] J. L. Garrett, D. Somers, and J. N. Munday, The effect of patch potentials in casimir force measurements determined by heterodyne kelvin probe force microscopy, J. Phys.: Condens. Matter **27**, 214012 (2015).

[70] T. F. Gallagher, *Rydberg Atoms* (Cambridge University Press, Cambridge, UK, 1994).

[71] A. Osterwalder and F. Merkt, Using High Rydberg States as Electric Field Sensors, Phys. Rev. Lett. **82**, 1831 (1999).

[72] S. D. Hogan, P. Allmendinger, H. Saßmannshausen, H. Schmutz, and F. Merkt, Surface-Electrode Rydberg-Stark Decelerator, Phys. Rev. Lett. **108**, 063008 (2012).

[73] C. Frugiuele, J. Pérez-Ríos, and C. Peset, Current and future perspectives of positronium and muonium spectroscopy as dark sectors probe, Phys. Rev. D **100**, 015010 (2019).

[74] M. S. Fee, A. P. Mills, Jr., S. Chu, E. D. Shaw, K. Danzmann, R. J. Chichester, and D. M. Zuckerman, Measurement of the Positronium $1\,^3S_1 \rightarrow 2\,^3S_1$ Interval by Continuous-Wave Two-Photon Excitation, Phys. Rev. Lett. **70**, 1397 (1993).

[75] D. Hanneke, S. Fogwell, and G. Gabrielse, New Measurement of the Electron Magnetic Moment and the Fine Structure Constant, Phys. Rev. Lett. **100**, 120801 (2008).

[76] E. Hardy and R. Lasenby, Stellar cooling bounds on new light particles: Plasma mixing effects, J. High Energy Phys. 02 (2017) 033.

[77] A. P. Mills, Jr. and G. H. Bearman, New Measurement of the Positronium Hyperfine Interval, Phys. Rev. Lett. **34**, 246 (1975).

[78] A. P. Mills Jr., Line-shape effects in the measurement of the positronium hyperfine interval, Phys. Rev. A **27**, 262 (1983).

[79] M. W. Ritter, P. O. Egan, V. W. Hughes, and K. A. Woodle, Precision determination of the hyperfine-structure interval in the ground state of positronium. V, Phys. Rev. A **30**, 1331 (1984).

[80] J. Khoury and A. Weltman, Chameleon Fields: Awaiting Surprises for Tests of Gravity in Space, Phys. Rev. Lett. **93**, 171104 (2004).

[81] C. Frugiuele, E. Fuchs, G. Perez, and M. Schlaffer, Constraining new physics models with isotope shift spectroscopy, Phys. Rev. D **96**, 015011 (2017).

[82] N. Arkani-Hamed, S. Dimopoulos, and G. Dvali, The hierarchy problem and new dimensions at a millimeter, Phys. Lett. B **429**, 263 (1998).

[83] E. J. Salumbides, A. N. Schellekens, B. Gato-Rivera, and W. Ubachs, Constraints on extra dimensions from precision molecular spectroscopy, New J. Phys. **17**, 033015 (2015).

[84] W. Ubachs, J. C. J. Koelemeij, K. S. E. Eikema, and E. J. Salumbides, Physics beyond the standard model from hydrogen spectroscopy, J. Mol. Spectrosc. **320**, 1 (2016).

[85] T. R. Weber, J. R. Danielson, and C. M. Surko, Electrostatic beams from tailored plasmas in a Penning-Malmberg trap, Phys. Plasmas **17**, 123507 (2010).

[86] D. A. Cooke, G. Barandun, S. Vergani, B. Brown, A. Rubbia, and P. Crivelli, Positron extraction to an electromagnetic field free region, J. Phys. B **49**, 014001 (2015).

[87] S. Chu and A. P. Mills, Jr., Excitation of the Positronium $1\,^3S_1 \rightarrow 2\,^3S_1$ Two-Photon Transition, Phys. Rev. Lett. **48**, 1333 (1982).

[88] M. Antonello, A. Belov, G. Bonomi, R. S. Brusa, M. Caccia, A. Camper, R. Caravita, F. Castelli, G. Cerchiari, D. Comparat, G. Consolati, A. Demetrio, L. Di Noto, M. Doser, M. Fanì, S. Gerber, A. Gligorova, F. Guatieri, P. Hackstock, S. Haider, A. Hinterberger, A. Kellerbauer, O. Khalidova, D. Krasnický, V. Lagomarsino, P. Lebrun, C. Malbrunot, S. Mariazzi, V. Matveev, S. R. Müller, G. Nebbia, P. Nedelec, M. Oberthaler, E. Oswald, D. Pagano, L. Penasa, V. Petracek, F. Prelz, B. Rienaecker, J. Robert, O. M. Røhne, A. Rotondi, H. Sandaker, R. Santoro, G. Testera, I. C. Tietje, E. Widmann, T. Wolz, P. Yzombard, C. Zimmer, and N. Zurlo (AEgIS Collaboration), Efficient $2\,^3S$ positronium production by stimulated decay from the $3\,^3P$ level, Phys. Rev. A **100**, 063414 (2019).

[89] A. Deller and S. D. Hogan, Microwave spectroscopy of the $1snp\,^3P_J$ fine structure of high Rydberg states in ^{4}He, Phys. Rev. A **97**, 012505 (2018).

[90] N. F. Ramsey, A new molecular beam resonance method, Phys. Rev. **76**, 996 (1949).

[91] N. F. Ramsey, Experiments with separated oscillatory fields and hydrogen masers, Rev. Mod. Phys. **62**, 541 (1990).

[92] A. C. Vutha and E. A. Hessels, Frequency-offset separated oscillatory fields, Phys. Rev. A **92**, 052504 (2015).